Numerical and Experimental Modeling of the Thermal Flow in a Modern Rotary Transfer Machine

Numerical and experimental modeling of the thermal flow in a modern rotary transfer machine

Francesco, Robusto[1]
Department of Industrial Engineering, University of Bologna
Viale del Risorgimento, 2
40136 Bologna, Italy
francesco.robusto@unibo.it

Dario, Croccolo
Department of Industrial Engineering, University of Bologna
Viale del Risorgimento, 2
40136 Bologna, Italy
dario.croccolo@unibo.it

Massimiliano, De Agostinis
Department of Industrial Engineering, University of Bologna
Viale del Risorgimento, 2
40136 Bologna, Italy
m.deagostinis@unibo.it

Stefano, Fini
Department of Industrial Engineering, University of Bologna
Viale del Risorgimento, 2
40136 Bologna, Italy
stefano.fini@unibo.it

Giorgio, Olmi
Department of Industrial Engineering, University of Bologna
Viale del Risorgimento, 2
40136 Bologna, Italy
giorgio.olmi@unibo.it

Marco, Rizzitelli
Bucci Industries
Via Mengolina 22 - 48018 Faenza (RA), Italy
m.rizzitelli@bucci-industries.com

[1] Corresponding author: Francesco Robusto (francesco.robusto@unibo.it).

Nicolò, Vincenzi
Bucci Industries
Via Mengolina 22 - 48018 Faenza (RA), Italy
n.vincenzi@bucci-industries.com

ABSTRACT

The aim of this study is to estimate the relative displacement between the spindle nose and the clamping vice in a rotary transfer machine due to temperature variations. The study was focused on the relative displacements caused by temperature variations produced by two heat sources: the environment around the machine and the 3-axis computer numerical control station during the duty cycle. Regarding the last point, an analytical model was developed, in order to account for different thermal sources inside the 3-axis module (e.g. ball screws, rolling bearings and guideways friction heat, as well as heat generation in the motor). The complete numerical model was calibrated and successfully validated. Comparison was run between numerical results and experimental data in the framework of trials involving a newly developed transfer machine. Finally, the complete model, considering the combination of both the heat sources, has made it possible to estimate spindle nose-clamp relative displacement during a typical working day, highlighting that the radial displacement risks affecting seriously the accuracy of a workpiece.

1. INTRODUCTION

The accuracy of a workpiece produced by a metal-cutting machine is generally affected by different factors: tool wear and tool deformation, holding fixture deformation and tool position error [1-4]. The error between the actual tool position and the ideally set one arises from geometric and kinematic issues as well as thermal variations. All the geometric, kinematic, and thermal errors are usually classified as quasi-static errors. Temperature variations lead to thermal deformation affecting

machine components, which implies a relative displacement between the tool and the clamp, and, consequently, the workpiece [5]. As highlighted in [6, 7], 70% of the total error is due to thermal displacement. Different approaches can be used, in order to reduce thermal errors, such as choosing materials with lower thermal expansion coefficients (e.g. cement concrete, fiber reinforced plastics etc.) [8-12]. A further method to reduce displacement due to thermal effects is making use of sandwich layouts in steel-composite hybrid structures [13]. However, on one hand, these strategies may actually reduce thermal displacements, but, on the other hand, are very expensive. According to [14, 15], different approaches can be used to model the thermoelastic behavior of machine tools and to compensate displacement errors. These approaches can be classified as phenomenological models, which use an empirical correlation between inputs (e.g. the external temperature) and outputs (e.g. temperature of the transfer machine) and numerical models that address the estimation of thermally induced errors, based on thermal load data [16]. The first ones are usually validated by experimental tests to be carried out under different environmental temperatures [11]. During the campaign, several duty cycles are performed, and the results are then fitted by regression models. Finite element numerical models generally lead to more reliable outcomes, as they have the capability of processing several thermal load sources, when many variables are involved. Machine tools are affected by considerable transient thermal flows that are highly not linearly variable both versus time and versus space; moreover, they depend on several factors, e.g. the environment or the performed working cycles etc. Therefore, thermal flow distribution is highly

complicated. Based on experimental and numerical data, it is possible to work out the actual temperature of the most critical machine groups [11] and, consequently, to properly correct the actual position of the working tool, based on the occurred thermal deflections. Experimental data are usually collected, monitoring the temperature of the critical area (by thermal sensors) and of the environment (by a thermometer).

The aim of the present study is to develop a finite element model, to validate it by experimental tests, and then to apply it as a predictive model, to simulate the thermal flow in a transfer machine under service condition. The importance of this procedure, in order to achieve a more accurate processing of workpieces, is also highlighted in another industrial case [6]. A further advantage of the proposed approach lies in its potentials: once validated, it may be used upon early design stage of similar machines. From this point of view, issues of novelty arise from the introduction of a methodology to address thermal displacement effects in machining centers. Determining thermal variations, assessing their effects on deformations and developing correction algorithms are key issues in modern tool machine design. This method is based on the integration of different source thermal loads to be used as inputs of a thermo-mechanical model of the machine. Focus was placed on thermal-structural simulations, which led to the prediction of the relative displacements between the spindle nose and the clamp and to its evolution versus time. Motivations of this study arise

2. MATERIALS AND METHODS

Thermal sources may be split into passive and dynamic sources [6,15]. In particular, a passive source deals with thermal loads arising from the environment. Conversely, a dynamic source consists in a thermal variation produced by sliding friction or by mechanical and electric powers needed during the duty cycle. The duty cycle consists in the implementation of a computer numerical control (CNC) operation list , t be regarded as part program. In the present study the same program was used for both production and experimentation. Thermal loads, due to passive and dynamic sources, were estimated experimentally by thermography, which is a non-destructive and non-invasive approach to thermal measurement [17]. A Ti-400 infrared thermal camera produced by ®Fluke (complying with the requirements of UNI CEI EN IS / IEC 17025) with uncertainty of ±2 °C was used for this purpose. The environmental temperature was measured by a digital thermometer. Numerical models were then developed to collect the data, addressing both the passive and the dynamic sources. It is worth mentioning the two models are not independent. In fact, the passive model has an influence on the dynamic one, as the convective coefficients affect the thermal flow between dynamic sources and the environment. Afterwards, the thermal-structural finite element (FE) analyses were carried out by ANSYS Workbench 17.2. An analytical model was developed by Matlab 2019 to provide inputs to the thermo-mechanical model. Finally, the numerical and analytical models were experimentally validated and were used for relative displacement prediction purposes.

2.1 Experimental procedure

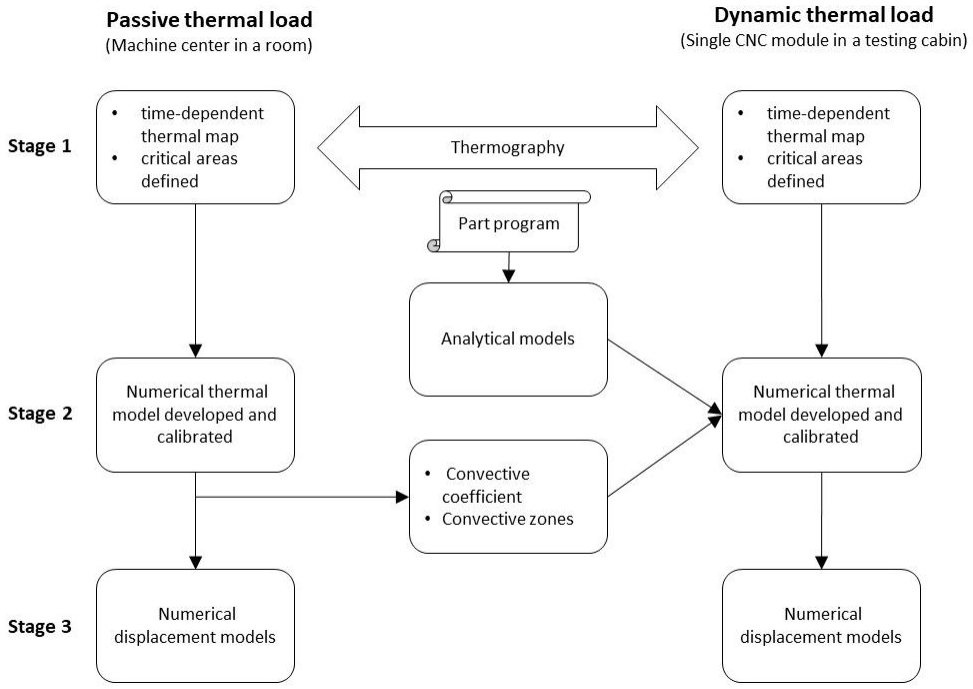

Fig. 1: Experimental procedure flow-chart

For the sake of clarity, the experimental procedure is graphically described in the flow-chart in Fig. 1: it can be split into the three stages detailed below. In the first one, a time-dependent thermal map of the most critical areas in the machining center was defined (critical areas are visible in Fig. 2). Data were collected by thermography, whereas a digital thermometer was placed near the machining center, in order to monitor the room temperature. Upon the second stage, numerical models were developed and calibrated, based on the experimental data retrieved at the previous step. During the last stage the numerical models were tuned to obtain the actual thermal evolution. In order to account for the effect of the passive source, the machine was divided into two macro zones (top and bottom as shown in Fig. 3) and two different

convective coefficients were used. The rationale for splitting the machine into these two parts arises from the two macro zones being separated by shaving conveyor. This component is not a thermal source but has an isolating effect, as it reduces air flow exchanges between the two parts. In addition, it must be remarked that the shaving conveyor may also isolate the lower part from the surrounding environment. Furthermore, the bottom part is usually shielded from the environment by additional fences that are needed to accomplish safety regulation. When considering the dynamic source, a calibration coefficient was introduced, as explained in Subsection 2.3, following a procedure that is well aligned to that applied in [6, 15]. Model calibration with respect to experimental data made it possible to drop down the error to 5%. Using passive and dynamic thermal sources as inputs for the thermo-mechanical model [16] finally led to the simulation of the relative displacement between the spindle nose and the clamp.

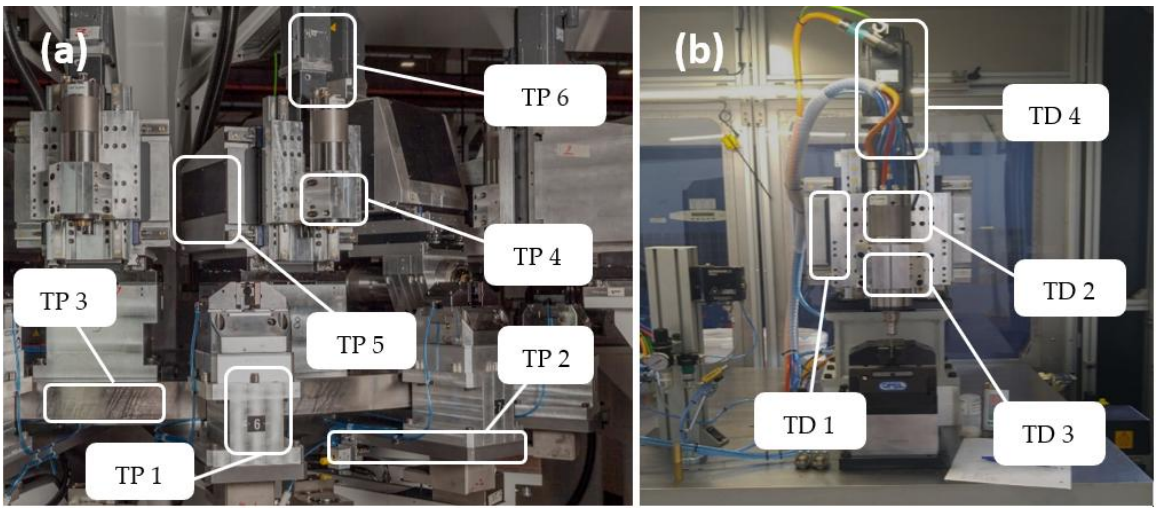

Fig. 2: (a) Working center with three CNC stations: the rectangular shapes indicate the critical zones, where the measurements were recorded for the thermal passive (TP) model. (b) Single 3-

axis CNC station in the testing room: the characteristic zones, where the thermal measurements were recorded are highlighted for the thermal dynamic (TD) model.

2.2 Passive thermal load

In the present study the proper determination of convective heat transfer coefficients (CHTC) is a key issue to correctly address the influence of the environmental temperature. It may be affected by many factors, such as fluid properties and velocity, shape and thermal condition of the surfaces, which produce a large variation over a wide range [18].

The top and the bottom zones of the machine exhibit different laminar flows and are therefore reasonably characterized by different convective coefficients. As highlighted in Table 1, CHTC at the bottom is lower than that at the top. The CHTCs values were calibrated by comparison between numerical results and the experimental data, in order to minimize the error within 2%. The coefficients obtained by this procedure are still in the range of non-turbulent regime, in agreement with [6].

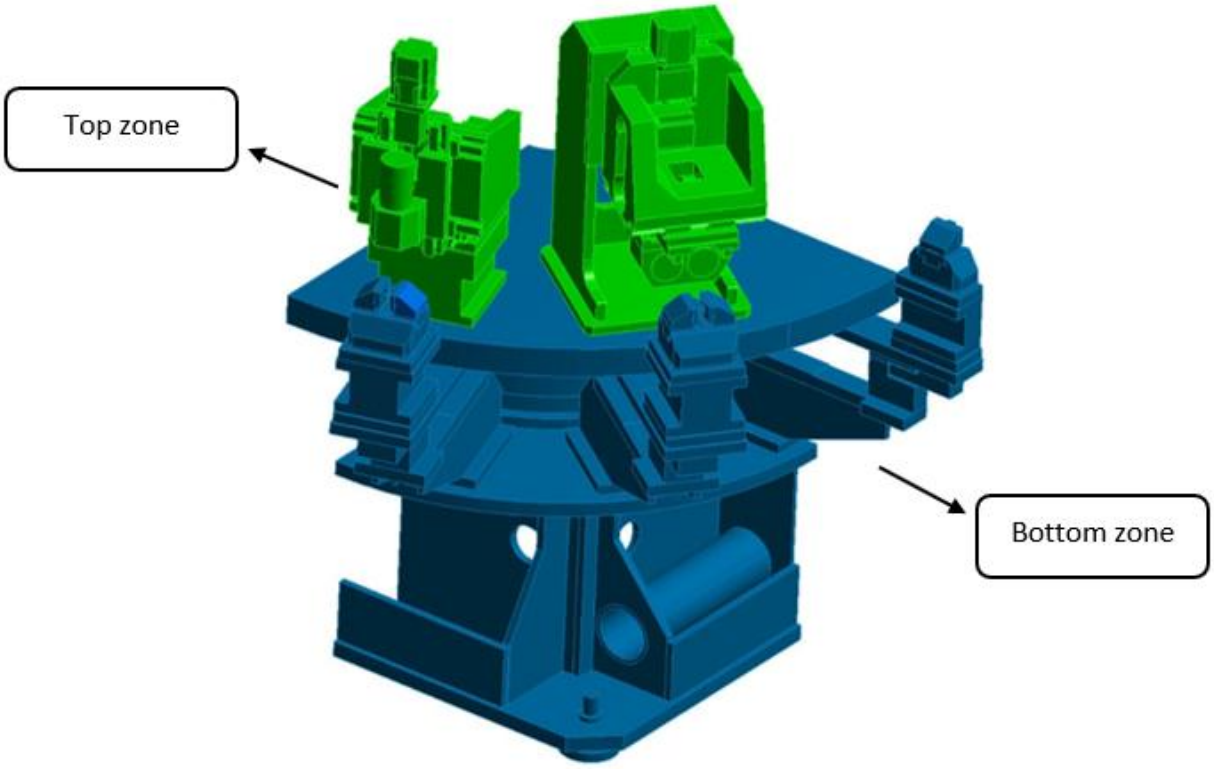

Fig. 3 – A quarter of the entire work center was split into two macro-zones.

Table 1 Theoretical coefficients for laminar flow in the different zones before and after calibration with respect to experimental data

Zone	Initial air calm coefficient	Corrected air calm coefficient
Top zone	$5\ W/m^2K$	$25\ W/m^2K$
Bottom zone	$5\ W/m^2K$	$3\ W/m^2K$

It could be argued that a large variation of the convective coefficients occurs before and after the experimental tuning. From this point of view, the performed calibration procedure is supported by the scientific literature, as in [6]. In this reference, some theoretical assumptions have initially been made regarding the convective coefficients that have been subsequently tuned by calibration. This procedure has led to considerable variations with coefficients being incremented even by a factor 4.3. Such

an increment appears to be consistent with the variation observed in the present study; moreover, convective coefficient variations over a wide range are also supported by remarks in [18]. The resulting large variation in terms of convective coefficients at the top and the bottom zones of the machine is indeed justified by the aforementioned isolation of the two zones being divided by the shaving conveyor that considerably reduces the airflow exchanges between these two parts. In addition, as remarked above, the bottom zone is also shielded from the environment by fences around the machine.

2.3 Dynamic thermal load

The experimental tests were carried out, involving a single three-axis CNC module (which is a part of the overall transfer machine), utilizing a testing cabin, whose temperature is referenced as Tcabin. This module was actuated continuously for 1 hour and the temperature level was monitored by the same part program used during the production phase. The part program consists of a sequence of instructions describing the tasks to be completed for machining a part. The instructions were arranged in the form required by a computer running under CNC software (e.g. tool start up point, cutting conditions, tool path, spindle speed, feed rate, coolant etc.). The commercial software used for the FE analyses does not allow for a thermal dynamic multi-body analysis. Therefore, in order to properly address kinematics-related thermal flows, a

numerical model was developed. It has the capability of estimating time-dependent thermal field distribution, taking each thermal dynamic source into account. Empirical literature formulas were implemented for this purpose, following the remarks in [6]. The functions "Heat flux" and "Internal heat generation" were used for this purpose. Combining these two functions, indeed, it is possible to simulate a variable thermal flow involving a specific surface or body. Moreover, the combination of these two functions is also suitable to simulate thermal power dissipation throughout machine service. The analytical models for thermal flow determination are reported in the next subsections. It must be pointed out the empirical formulas to be implemented in these models need some coefficients, based on the recommendations by technical handbooks. This point clearly introduces a bias in the numerical models. Therefore, these models had to be finally calibrated by comparison to experimental data and were then successfully validated by a specific experiment (in machining center warmup conditions).

2.3.1 Frictional heat calculation – roller monoguides

According to [6], the thermal power dissipated due to friction (PG) can be determined by Eq. 1:

$$P_G = \mu \cdot F \cdot v \tag{1}$$

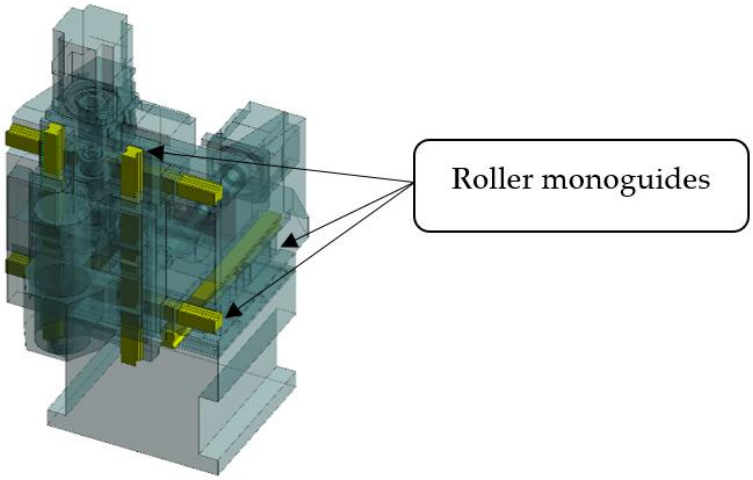

Fig. 4 – The roller monoguides in a single 3-axis CNC module, highlighted in yellow

The utilized symbols have the following meanings: μ is the friction coefficient, F is the force acting on the roller monoguides, whereas v is the relative speed between the bodies in contact. The friction coefficient (μ) was estimated as $4 \cdot 10^{-4}$, according to [19]. The total force on the roller monoguides (F) can be calculated by Eq. 2 according to [20]:

$$F = 2F_{pr} + \frac{1}{3} \cdot F_{load} \tag{2}$$

The operating load (F_{load}) considers how structure weight is split into roller monoguides. This load is presumed to be applied on the center of mass (Fig. 5). The preload force (F_{pr}) can be computed by Eq. 3 according to [21]:

$$F_{pr} = 0.13 \cdot F_{load} \tag{3}$$

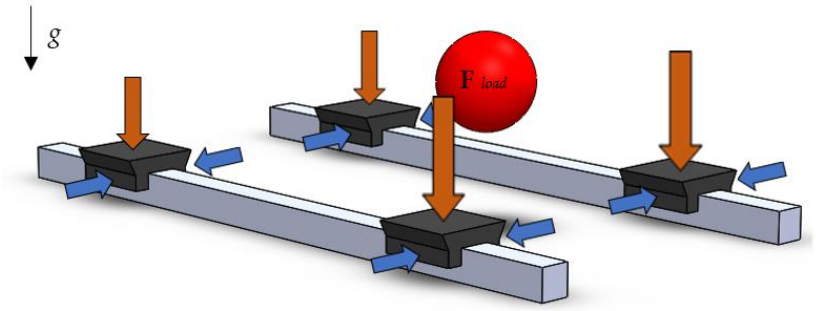

Fig. 5 - Example of load distribution on a couple of roller monoguides (F_{load} is represented by red arrows, F_{pr} by blue arrows)

2.3.2 Rolling bearing heat calculation

Standard ISO 15312 [22] was used to estimate heat generation in rolling bearings (P_{RB}), as follows (Eq. 4):

$$P_{RB} = 10^{-3} \cdot \pi \cdot n_\theta \cdot (M_{0r} + M_{1r}) \tag{4}$$

Where n_θ is the rotational speed, M_{0r} is the load-independent frictional moment and M_{1r} is the load-dependent frictional moment under the reference condition at the thermal rotational speed.

M_{0r} takes viscous friction in the bearing into account and depends on the rolling bearing type, size, speed, and lubrication condition. It can be calculated by Eq. 5 according to [22]:

$$M_{0r} = 10^{-7} \cdot f_{0r} \cdot (\nu_r \cdot n_\theta \cdot 60)^{\frac{2}{3}} \cdot {d_m}^3 \tag{5}$$

In this formula f_{0r} is the viscous coefficient, ν_r indicates the viscosity of the lubricant and d_m is the mean diameter of the rolling bearing.

The viscous coefficient (f_{0r}) depends on the bearing type and on the actual contact angle: it was set to 2 (for this case study) according to [22].

The load-dependent frictional moment (M_{1r}) was finally calculated by Eq. 6, where f_{1r} is the load factor equal to 2.5·10-4, whereas P_{1r} is the reference load to be regarded as 2% of the static axial bearing load [22].

$$M_{1r} = f_{1r} \cdot P_{1r} \cdot d_m \tag{6}$$

2.3.3 Ball-screws heat calculation

The ball-screws thermal power generation (P_{BS}) can be estimated by Eq. 7, according to [23] and [24]:

$$P_{BS} = \pi \cdot n_\theta \cdot (M_d + M_{pl}) \tag{7}$$

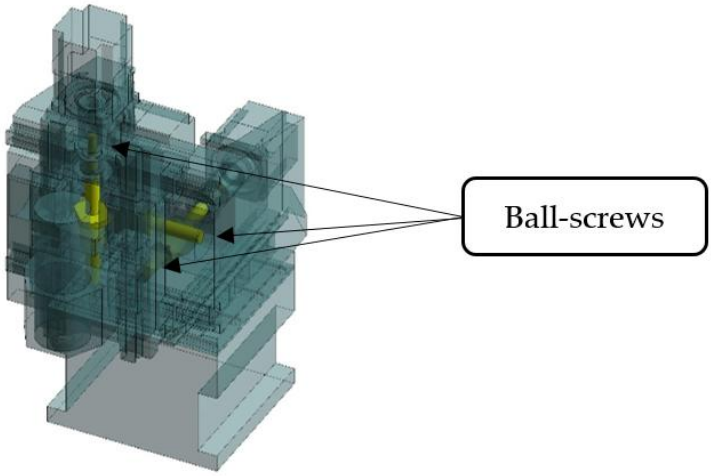

Fig. 6 - The Ball-screws in a single 3-axis CNC module, highlighted in yellow

In this formula M_d is the frictional moment produced by the external load (calculated by Eq. 8) and M_{pl} is the frictional moment produced by the preload (yielded by Eq. 9).

$$M_d = F_{ext} \cdot L \cdot \frac{1-\eta_{BS}}{2 \cdot \pi} \tag{8}$$

$$M_{pl} = F_p \cdot L \cdot \frac{1-\eta_{BS}{}^2}{2 \cdot \pi} \tag{9}$$

F_{ext} indicates the external load applied on the screw, whereas L is the pitch of the screw, η_{BS} is the screw efficiency and F_p is the preload force reported in the ball screw catalogue (in this case 683.6 N). The efficiency η_{BS} accounts for the amount of energy being lost, when rotary motion is turned into translational motion and vice versa: it can be calculated by Eq. 10:

$$\eta_{BS} \cong \frac{\tan(\varphi)}{\tan(\varphi+\rho)} \tag{10}$$

In this equation φ is the helix angle, whereas ρ is the friction angle.

2.3.4 Axis motor heat calculation

The thermal power dissipation due to mechanical (e.g. frictional) losses (P_{mec}), can be evaluated as follows (Eq. 11), according to [25]:

$$P_{mec} = \pi \cdot n_\theta \cdot T_{shaft} \cdot (1-\eta_{mec}) \tag{11}$$

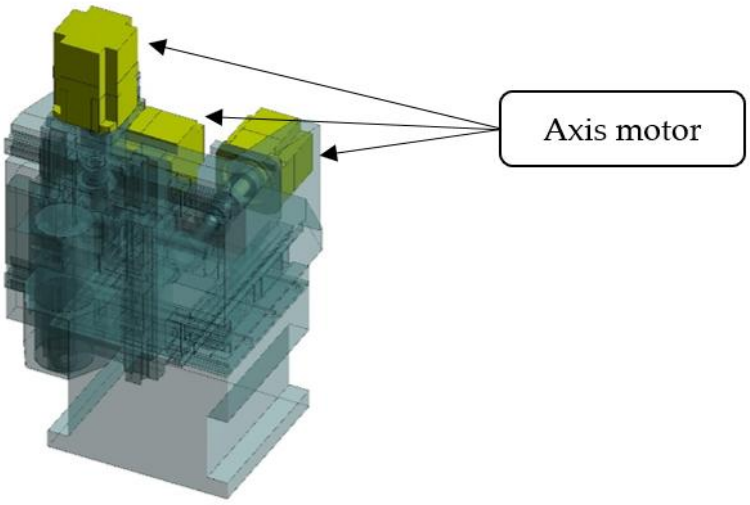

Fig. 7 - Axis motor in a single 3-axis CNC module, highlighted in yellow

Where T_{shaft} is the total torque acting on the engine shaft and η_{mec} is the motor mechanical efficiency.

The amount of electric power (P_{ele}) being dissipated due to the Joule effect is the most relevant contribution to be considered, in order to determine the overall heat dissipation of the motor. This term was evaluated by Eq.12 according to [26]:

$$P_{ele} = \left(\frac{T_{mot}}{\xi} \right) \cdot \left(n_{\theta} \cdot \varepsilon \right) \tag{12}$$

T_{mot} is the total torque required by the electric motor, ξ is the electric current constant and ε is the electric voltage constant.

The total motor thermal power generation is yielded by the sum of the aforementioned contributions, as highlighted in Eq.13:

$$P_{tot} = P_{mec} + P_{ele} \tag{13}$$

2.4 FE model

After experimentally calibrating the dynamic thermal loads, they were used as inputs for the development of the transient thermo-structural analysis of the entire machine. For this purpose, passive thermal loads were used as well. The symmetry condition was applied to a quarter of the machine. In the FE model, 147,190 tetrahedral elements (SOLID187) were used, for a total amount of 289,793 nodes.

According to the method proposed in [27], uniform, coarse, global meshes can be used to obtain a sufficiently accurate solution. Therefore, there is no need to refine meshes, which results in a lower computational effort. The default adaptive element sizing was applied to the entire body, except for the sheet metal case highlighted in Fig. 8, for which a 25 mm-sized element was chosen.

The boundary conditions were set up using pre-defined functions: “convection” to impose the passive thermal load as highlighted in Subsection 2.2; "heat flux" and "Internal heat generation" to apply the dynamic thermal loads in the thermal analysis as highlighted in 2.3. In order to run the thermo-mechanical analysis, the aforementioned thermal loads were used as inputs, modelling the supports at the machine base as fixed constraints. Furthermore, bonded connections were generally used, except for the roller monoguides, where a no-separation contact was introduced.

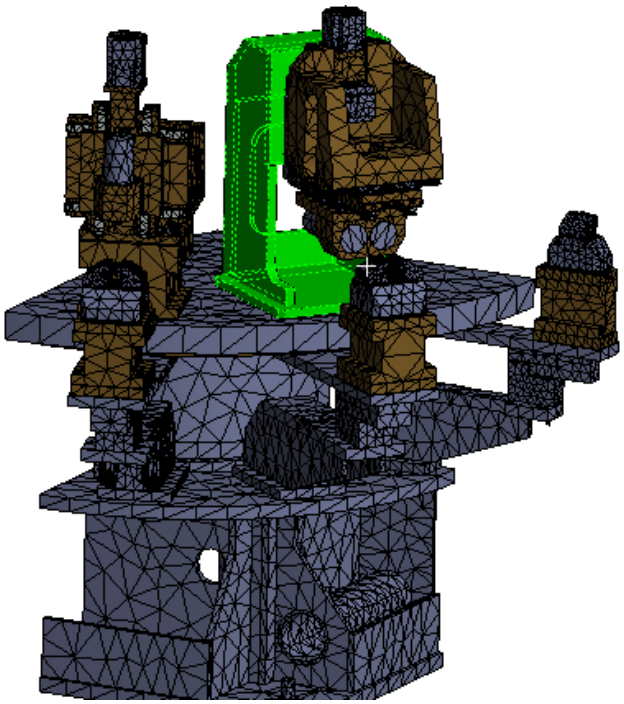

Fig. 8 – A meshed quarter of the entire machining center. The highlighted sheet metal case was meshed by a different strategy (manual sizing method)

3. RESULTS AND DISCUSSION

The results of both the passive and the dynamic models are reported here. For the sake of clarity, they are divided into subsections.

3.1 Passive thermal model

The overall experimental thermal map involving all the analyzed zones is shown in Fig. 9. This plot displays the evolution versus time of the temperature at each sampling area on the machine. It is worth mentioning the sampling zones can be split into two macro areas: bottom and top of the machine. As highlighted in Fig. 2, TP1, TP2 and TP3 are the temperatures at the machine bottom side, whereas TP4, TP5 and TP6 are the temperatures at the top. Temperature trends for these two zones are separated

by the room temperature (T_{env}). Moreover, the bottom area temperature (TP1, TP2, TP3) trend looks directly affected by room temperature variation versus time. Whereas temperature distribution at the top (TP4 and TP6) is likely to be more affected by other thermal sources, such as electronic control components. These components, which are typically located at the top part of the machine, are the first ones to be switched on upon the warmup stage. Consequently, due to Joule effect power dissipation, they produce a rapid heating of the entire upper macro zone. As a matter of fact, as Tenv increases, TP 6 and TP4 areas exhibit a nearly constant trend versus time, whereas the temperature distributions at the bottom side follow the trend of Tenv.

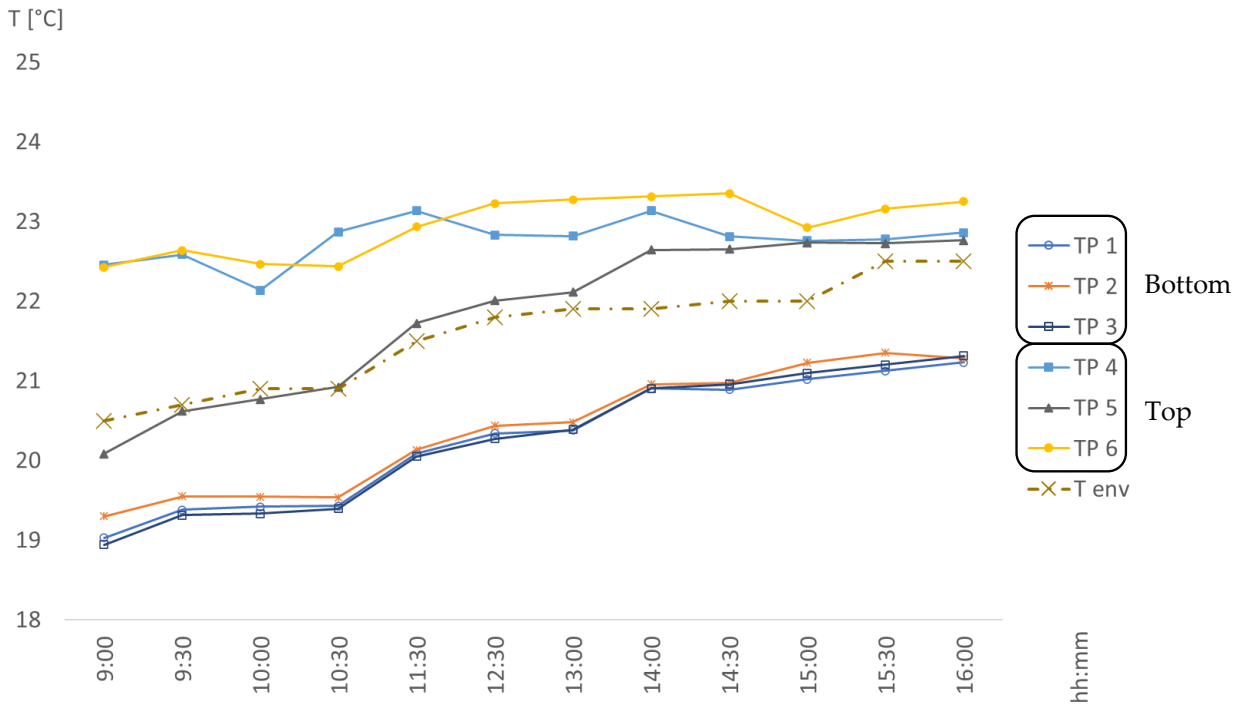

Fig. 9: Global thermal trend of the critical areas (depicted in Fig. 2) with environment temperature trend

As an example, Fig. 10 collects the trends of the experimental and simulated data for the TP2 region, accounting for numerical data before and after model calibration (convective coefficient tuning).

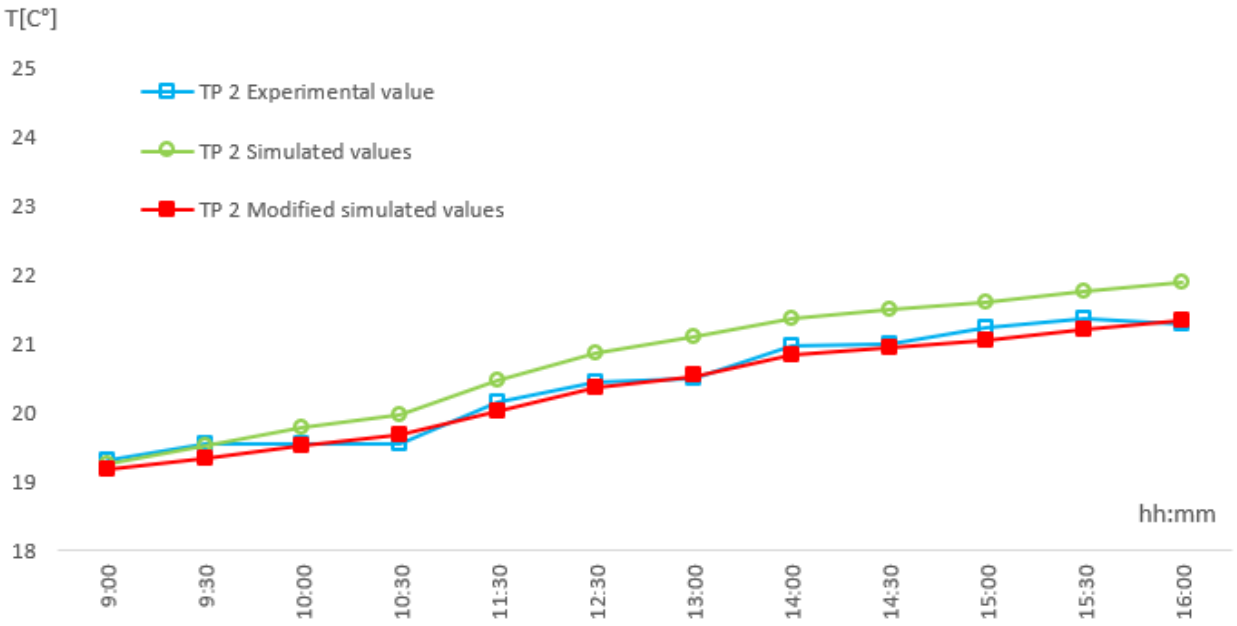

Fig. 10: Experimental and simulated (before and after calibration) temperature values during a working day in the TP 2 zone at the bottom side

The results concerned with passive thermal loads, yielded by the present thermal simulation, following convective coefficient tuning, were then used as inputs for the implementation of a static structural analysis. This preliminary numerical model, which does not account for dynamic thermal loads, made it possible to evaluate the relative displacement between the spindle nose and the clamp. The results are displayed in two different reference systems. Vertical displacements are provided in Fig. 11, whereas the radial displacements are shown in Fig. 12. These displacements would be indeed too high to warrant the required accuracy for the workpiece. Anyway, this outcome has the basic role of being the input for an algorithm that is able to correct the

applied motions, thus compensating the occurred thermal relative displacements. It was not possible to run an experimental validation of the numerical model, as it would have required a comparator with very high sensitivity in the order of micrometer. Moreover, provided that an instrument with a sufficient sensitivity could be made available, the yielded measurement would be affected by the thermal deformation of the measuring device support. In fact, this would be located in the same environment and would consequently be affected by the same temperature changes. This occurrence makes the experimental validation almost impossible in this case.

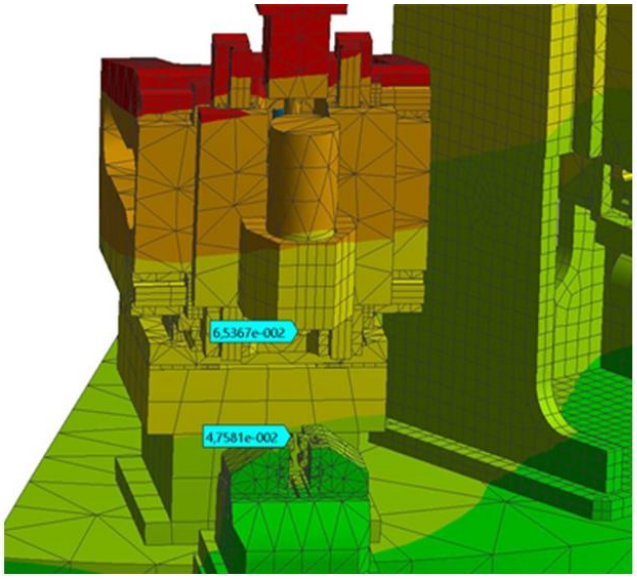

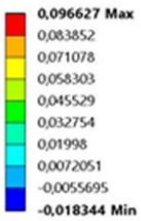

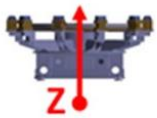

Axial deformation (ΔT_{env}~3 C° in 8h)		Relative displacement
Spindle nose	0,065 (mm)	0,017 (mm)
Clamp	0,048 (mm)	

Fig. 11: Vertical displacement (z axis) results

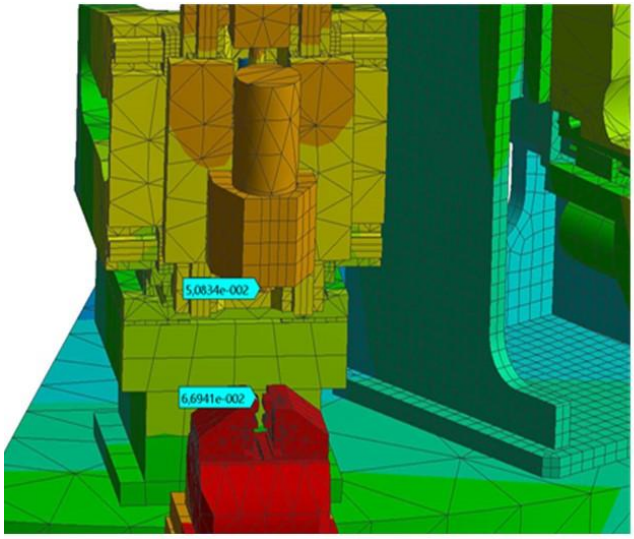

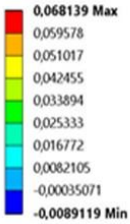

Radial deformation (ΔT_{amb}~3 C° in 8h)		Relative displacement
Spindle nose	0,051 (mm)	0,016 (mm)
Clamp	0,067 (mm)	

Fig. 12: Radial displacement (x axis) results

The calibrated model was then used to predict temperature evolution versus time in the most relevant machine zones, considering a higher environmental temperature variation with respect to the experimental trial. In particular, during testing, temperature variation was around just 3 C° (Fig. 10), whereas, taking advantage of the calibrated model, it was possible to extend thermal response estimation over a 15 C° range. The results for the latter increment are shown in Fig. 13: it can be pointed out the model exhibits a linear behavior, which suggests the relative displacements also have a linear behavior.

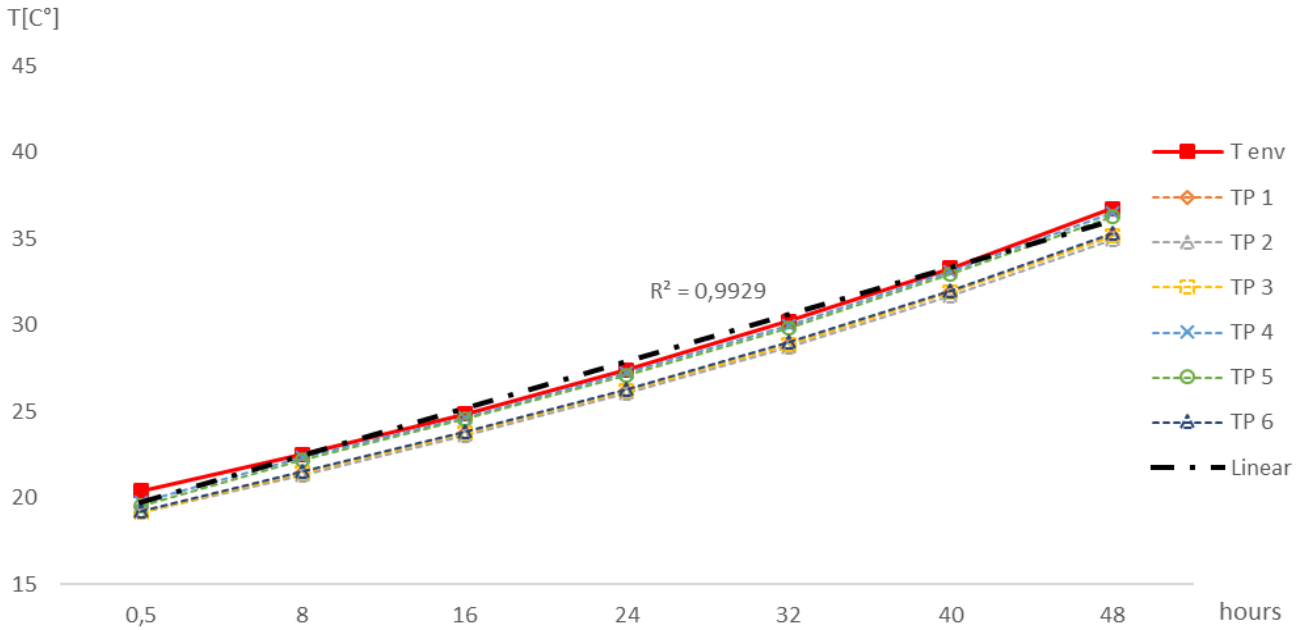

Fig. 13: Global trend with reference to the thermal critical areas highlighted in Fig. 1

3.2 Dynamic thermal model

At the beginning of the test, the temperatures in the analyzed areas proved to be higher than that in the environment. Thus, the initial hypothesis was that the lighting system and the spindle cooling system (SCS) were affecting the test outcomes, because they were placed in the neighborhood of the testing cabin. For example, the SCS generates heat to keep the cooler at its working temperature. Therefore, in order to allow for experimental vs. numerical result comparison, the data shown in this Section are normalized with respect to the initial temperature T_start that is different for each involved body.

The comparison between the experimental and the simulated calibrated results for one of the most representative areas (the front carriage plate -TD 1) is shown in Fig. 14. The trend indicates that ball-screw bearing friction causes a very small temperature

increment. Moreover, the numerical model for this zone reliably describes the actual trend and the error is lower than 1%.

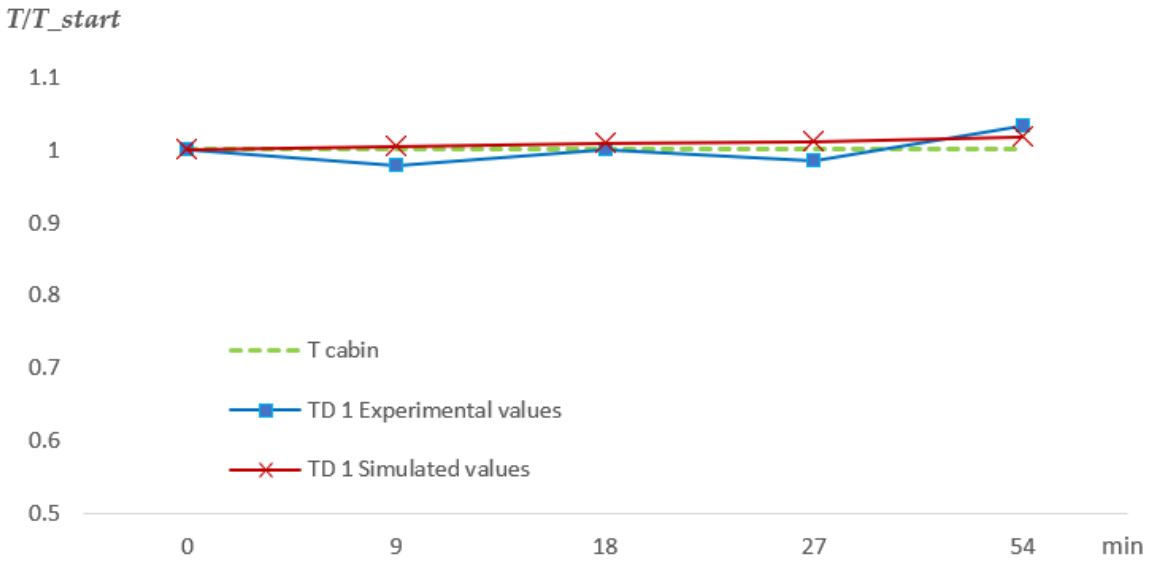

Fig. 14: Comparison between the experimental and numerical yields with regard to the thermal dynamic zone 1 (TD 1)

The analysis conducted in the vicinity of the z-axis motor (TD 4) highlighted a linear heating trend versus time (Fig. 15). It is worth mentioning the calibrated numerical values closely match the experimental ones (Red line).

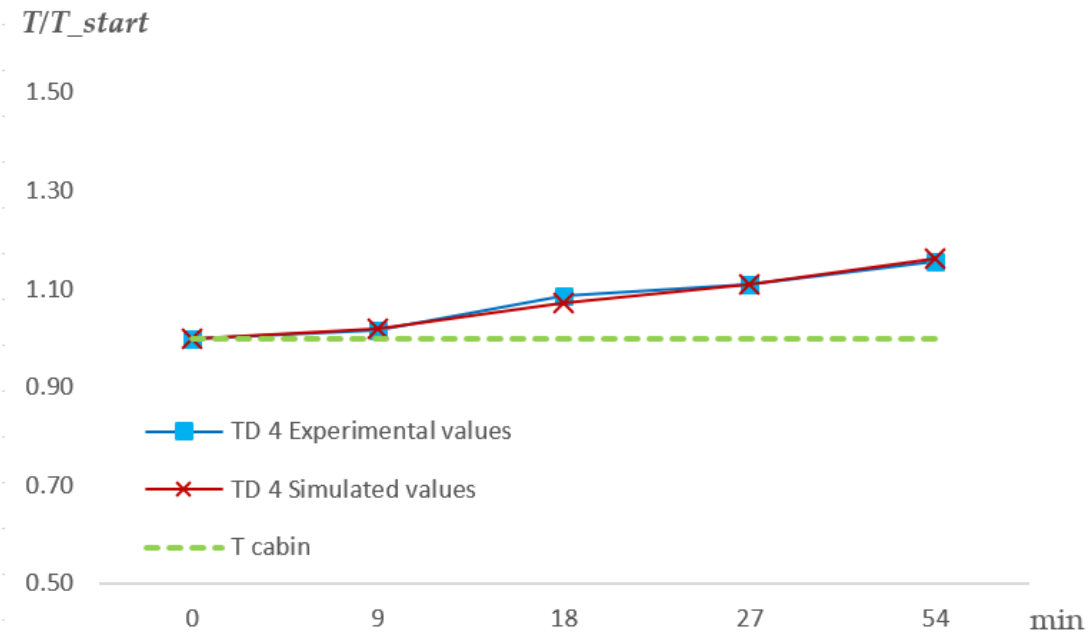

Fig. 15: Comparison between the outcomes of the experimental and numerical models with reference to the thermal dynamic zone 4 (TD 4)

In order to validate the aforementioned numerical model of the motor, including the previously calibrated convective coefficients, a further test was specifically carried out. During the experiment, the CNC module worked for 140 minutes. This analysis is usually performed, to evaluate the warmup duration until a steady-state condition is achieved by the machine. During this time interval, the machining center executes the part program without the workpiece until thermal equilibrium is finally reached. The experimental results and the numerical ones are plotted together in Fig. 16. In this case, the retrieved maximum error was 0.5%: therefore, it could be concluded that the numerical model was validated.

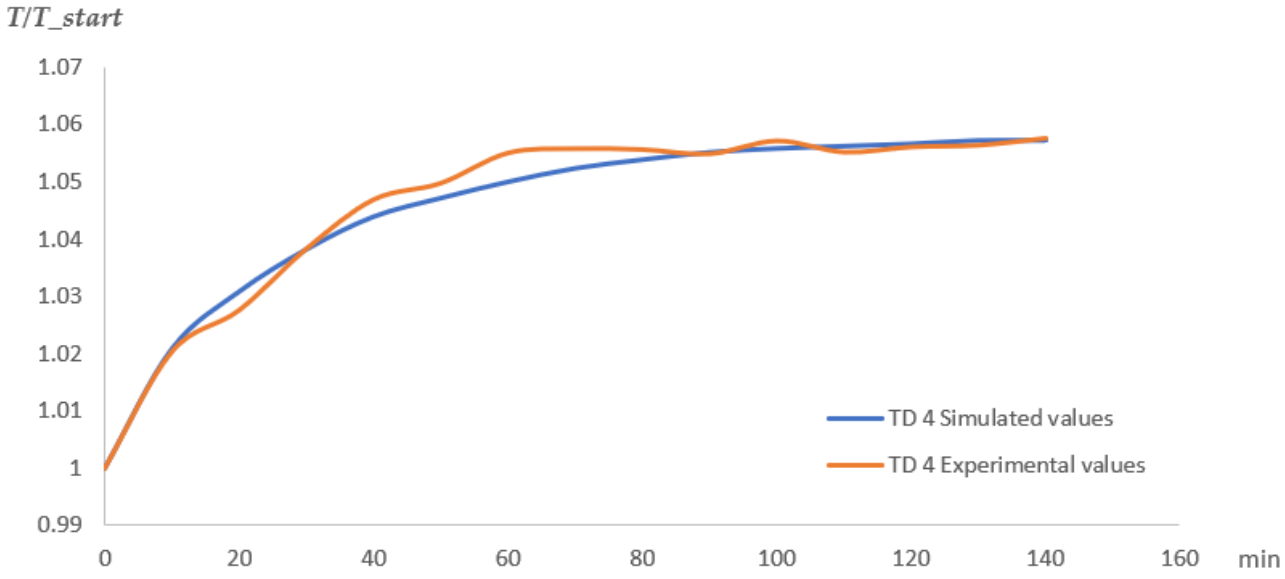

Fig. 16: Thermal dynamic zone TD 4 temperature: comparison between the experimental and the numerical results in the framework of an extended duration warmup test (140 minutes)

3.3 Dynamic Thermo-Mechanical model

The results of the thermal simulations, in terms of temperature variation versus time, were then used for the implementation of the structural analysis that yielded the relative displacement between the spindle nose and the clamp. The results of these simulations are provided in Fig.s 17 and 18. In particular, the vertical displacement is shown in Fig. 17, whereas the radial shift is displayed in Fig. 18. It is necessary to point out that, as an effect of the incorporation of dynamic thermal changes into the conducted analysis, displacement distributions are different. Assuming to place a reference point on the spindle nose, one can observe two different trends versus time for the relative displacement with respect to the clamp in the axial (z) and in the radial directions (r). Looking at Fig. 17, it can be highlighted the relative axial displacement tends to zero after a transient, thus restoring the initial relative position, whereas the radial displacement (Fig. 18) tends to increase, which leads to a divergent relative

position. From this point of view, an important result is that in steady conditions after warmup the vertical relative displacement does not significantly affect the accuracy of the workpiece. On the other hand, relative displacement in the radial direction is likely to have a detrimental effect on the machining process, since it tends to diverge for increasing working time. Therefore, the machine embedded compensation algorithm must be focused on the relative displacement reduction along this direction.

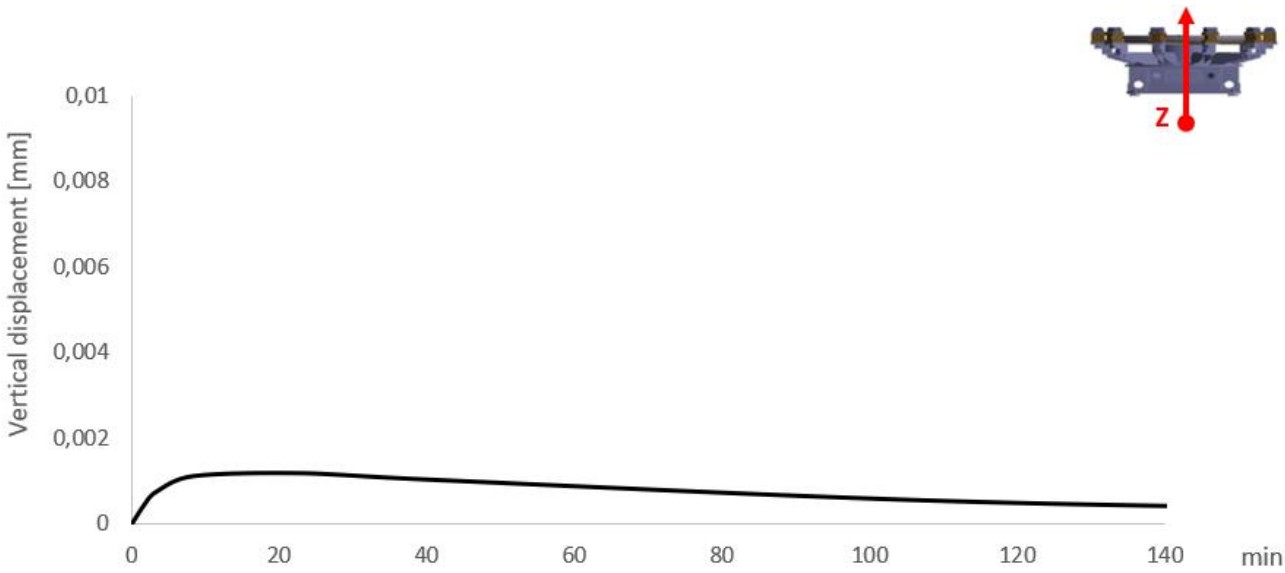

Fig. 17 - Structural analysis results in terms of relative vertical displacement

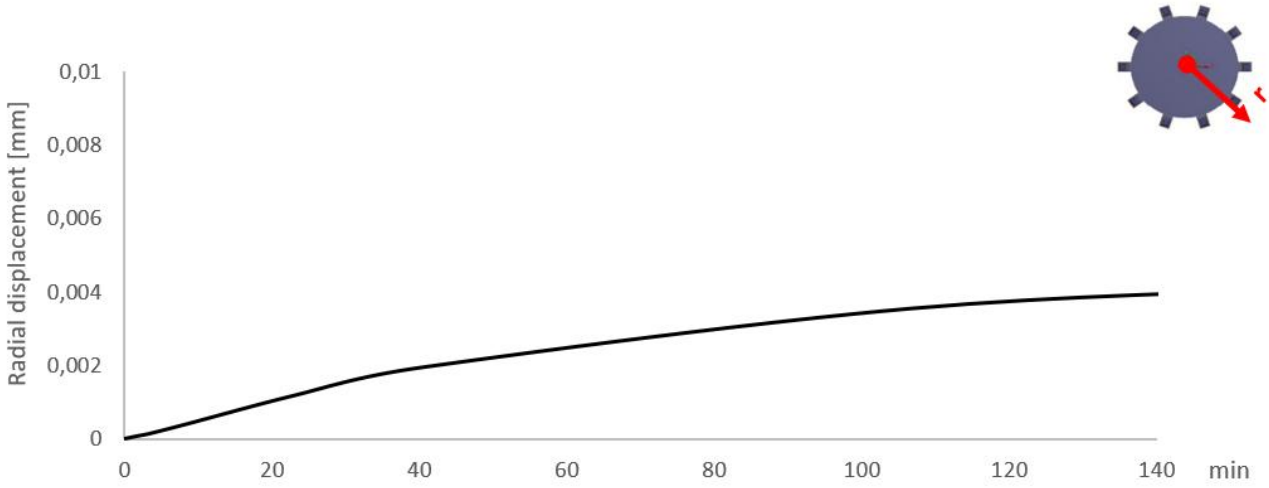

Fig. 18 - Structural analysis results in terms of relative radial displacement

The behaviors observed in Fig. 17 and Fig. 18 could be explained focusing on the materials used to build the machine (shown in Fig. 19). These materials have a different thermal expansion coefficient and. therefore, the combination of their displacements leads to a different behavior in the axial and radial directions. A further reason arises from dimensional and geometrical issues: in a transfer machine the extension of its components, with particular regard to the rotary plate, along the radial direction is remarkably higher than that in the vertical direction. In other words, the prevailing dimension is radial rather than vertical. As a consequence, it is reasonable that the rotary plate is affected by a high thermal deformation in the radial direction, which also reflects in a much higher relative displacement in the same direction. On the other hand, deformations along the vertical axis are generally lower and tend to compensate each other after a transient as an effect of a compensation of different material expansions.

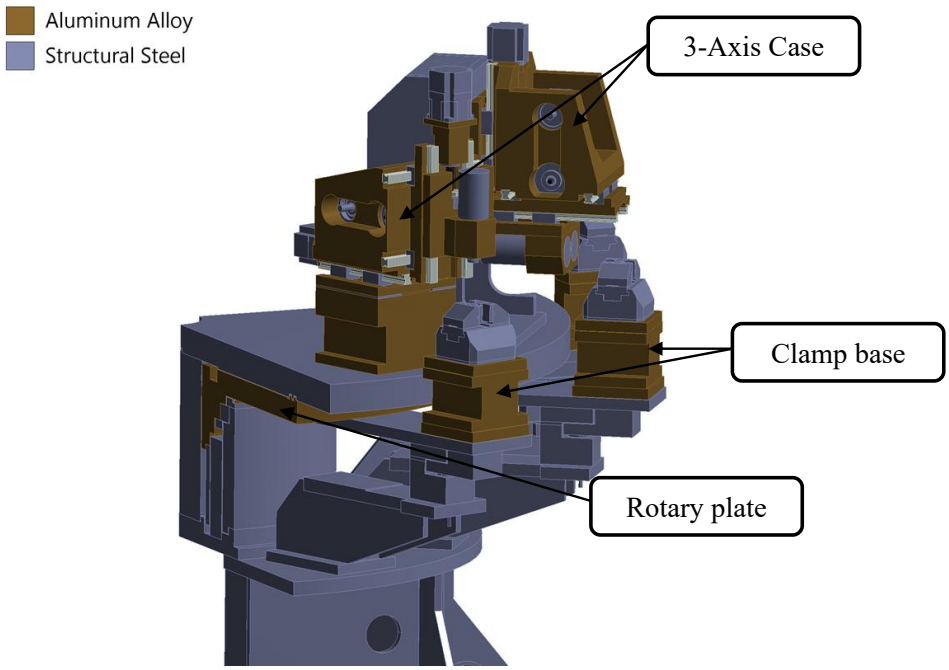

Fig. 19 - A section view of the machining center, where the materials used for component manufacturing are highlighted.

4. CONCLUSIONS

The main purpose of the study was to develop a methodology for the determination of the relative position between the spindle nose and the clamp due to a surrounding temperature variation. This method is based on the estimation of the passive and dynamic thermal loads, which requires an experimental calibration for the first ones, and analytical computations by suitable formulas for the second ones. These loads are used as inputs for a dynamic thermo-mechanical numerical model that, following experimental validation, may be used for relative displacement estimation (and subsequent correction by a suitable algorithm) in several industrial cases.

The machining center temperature was experimentally measured under different conditions. Analytical and numerical models were developed as well, in order to simulate the thermal machine behavior. Both the analytical and numerical models were tuned, in order to achieve accurate results and to reduce the scattering with respect to the experimental results. The passive models made it possible to determine that the spindle nose-clamp relative displacement exhibits a linear behavior. Moreover, the developed numerical model provided an accurate estimation of the actual displacement after a temperature variation. A further analysis at incremented time was carried out, which led to the calibration and validation of the dynamic model, thus also estimating the warmup duration of the studied machining center.

Two different trends over time were estimated by the complete dynamic thermo-mechanical model for the relative displacement of the nose of the spindle with respect to the clamp in the axial and in the radial directions. As a matter of fact, the relative axial displacement tends to zero after a transient, thus restoring the initial relative position, whereas the radial displacement tends to increase. This result will make it possible to optimize the machine embedded motion algorithm, focusing on corrections in the radial direction.

FUNDING

Italian Ministry of Economic Development (MISE) - Spesa agevolata con il Bando Accordi per l'Innovazione - Cod CUP B21B19001120008

NOMENCLATURE

P_G	Roller monoguide thermal power	[W]
μ	Friction coefficient on the roller monoguide	1
F	Force acting on the roller monoguide	[N]
ν	Relative speed between the bodies in contact	[m/s]
F_{load}	Operating load on the roller monoguide	[N]
F_{pr}	The preload force on the roller monoguide	[N]
P_{RB}	Rolling bearings thermal power	[W]
n_θ	Rotational speed of the rolling bearing	[s^{-1}]
M_{0r}	Load-independent frictional moment of the rolling bearing	[Nmm]
M_{1r}	Load dependent frictional moment under the reference condition at the thermal rotational speed of the rolling bearing	[Nmm]
f_{0r}	Coefficient for the load-independent frictional moment for the reference condition of the rolling bearing	1
ν_r	Kinematic viscosity of the lubricant under the reference conditions of the rolling bearing	[mm^2/s]
d_m	Mean diameter of the rolling bearing	[mm]
f_{1r}	Coefficient for the load-dependent frictional moment for the reference condition of the rolling bearing	1

P_{1r}	Reference load on the rolling bearing	[N]
P_{BS}	ball-screws thermal power	[W]
M_d	Frictional moment produced by the external load on the screw	[Nm]
M_{pl}	Frictional moment produced by pre-load on the screw	[Nm]
F_{ext}	indicates the external load applied on the screw	[N]
L	pitch of the screw	[m]
η_{BS}	The screw efficiency	1
F_p	Preload force reported in the ball screw catalogue.	[N]
φ	The helix angle of the screw	[°]
ρ	The friction angle	[°]
P_{mec}	The thermal power dissipation due to mechanical losses	[W]
T_{shaft}	Total torque acting on the engine shaft	[Nm]
η_{mec}	The motor mechanical efficiency	1
P_{ele}	The amount of electric power being dissipated due to the Joule effect	[W]
T_{mot}	The total torque required by the electric motor	[Nm]
ξ	The electric current constant	1
ε	The electric voltage constant.	1

P_{tot}	The total motor thermal power generation	[W]

REFERENCES

[1] Vilmos, V. S., 2008, "Machine-Tool Settings to Reduce the Sensitivity of Spiral Bevel Gears to Tooth Errors and Misalignments", Journal of Mechanical Design, vol. **138**(8), pp. 0826031 - 08260310.

[2] Croccolo, D., Cavalli, O., De Agostinis, M., Fini, S., Olmi, G., Robusto F. and Vincenzi, N., 2018, "A Methodology for the Lightweight Design of modern transfer machine tools" Machines, **6**(1).

[3] Pegna, J., 1997, "Generalized Abbe Principle: Position Error Propagation in Machine Elements", Journal of Mechanical Design, **119**(1), pp. 1-7.

[4] Franco, P., Estrems, M. and Faura, F., 2008, "A study of back cutting surface finish from tool errors and machine tool deviations during face milling", International Journal of Machine Tools and Manufacture, **48**(1), pp. 112-123.

[5] Ramesh, R., Mannan, M. A. and Poo, A. N., 2000, "Error compensation in machine tools — a review Part II: thermal errors", International Journal of Machine Tools and Manufacture, **40**(9), pp. 1257-1284.

[6] Xiaobo, M., Kuanmin, M., Fengyun, W., Bo, Y. and Sheng, L., 2018, "A convective heat transfer coefficient algorithm for thermal analysis of machine tools considering a temperature change", International Journal of Advanced Manufacturing Technology, **99**(5-8), pp. 1877-1889.

[7] Lee, J. H., and Yang, S. H., 2002, "Statistical optimization and assessment of a thermal error model for CNC machine tools", International Journal of Machine Tools and Manufacture, **42**(1), 147-155.

[8] Kim, J.D. and Kim, D.S., 1997, "Development and application of an ultra-precision lathe", International Journal of Advanced Manufacturing Technology, **13**(3), pp. 164-171.

[9] Tanabe, I., Takada, K., and Tsutsumi, M., 1986, "Thermal deformation of machine tool structures using epoxy resin concrete", *Proceedings of the Twenty-Sixth International Machine Tool Design and Research Conference*, pp. 245-252.

[10] Kim, H.S., Jeong, K.S., and Lee, D.G., 1997, "Design and manufacture of a three-axis ultra-precision CNC grinding machine," Journal of Materials Processing Technology, vol. **71**(2), pp. 258-266.

[11] Nishiyama, H., Nagayasu, O., Shin-Nou, T., Sato, H., O-Hori, M. and Sugishita, H., 1988, "Development of concrete machining centre and identification of the dynamic and

the thermal structural behaviour", CIRP Annals - Manufacturing Technology, **37**(1), pp. 377-380.

[12] Nymoen, H., Benzinger, K., Paluncic, Z., Hoffmann, E., and Spur, G., 1988, "Thermal behaviour optimisation of machine tools", CIRP Annals, **37**(1), pp. 401-105.

[13] Do Suh, J., and Gil Lee, D., 2004, "Thermal characteristics of composite sandwich structures," Composite Structures, **66**(1-4), pp. 429-438.

[14] Gebhardt., M, 2014, Thermal behaviour and compensation of rotary axes in 5-axis machine tools, PhD Thesis, University of Bayreuth, ETH-Zürich.

[15] Dos Santos, M. O., Batalha, G. F. , Bordinassi, E. C., and Miori, G. F., 2018, "Numerical and experimental modeling of thermal errors in five-axis CNC machining center," International Journal of Advanced Manufacturing Technology, **96**(5-8), pp. 1619-1642.

[16] Liu, K., Li, T., Wang, Y., Sun, M., Wu, Y., & Zhu, T. (2018). “Physically based modeling method for comprehensive thermally induced errors of CNC machining centers”, *The International Journal of Advanced Manufacturing Technology*, *94*(1-4), pp. 463-474.

[17] Bagavathiappan, S., Lahiri, B. B., Saravanan, T., Philip, J., & Jayakumar, T. (2013). “Infrared thermography for condition monitoring–A review”, Infrared Physics & Technology, 60, pp. 35-55.

[18] Tan, F., Yin, Q., Dong, G., Xie, L., & Yin, G. (2017). “An optimal convective heat transfer coefficient calculation method in thermal analysis of spindle system.” The International Journal of Advanced Manufacturing Technology, 91(5-8), pp. 2549-2560.

[19] Rexroth Bosch Group, Ball Rail Systems, 2018.

[20] Utica, G. (2012). “Caratterizzazione dell’attrito nelle guide lineari a ricircolo di rulli attraverso prove sperimentali per lo sviluppo della modellazione FEM”. Master Thesis, Politecnico di Milano, Milan-Italy

[21] Rosa Sistemi, MG Monoguide recirculating linear rollers bearing, 2015.

[22] ISO 15312:2018, "Rolling bearings — Thermal speed rating — Calculation". 2018.

[23] Servomech, Ball screws and nuts, 2017.

[24] Oyanguren, A., Ulacia, I., Larranaga, J., Gallo, A., Arana, A. and Gonzalez, R., 2013, "Prediction of heat generation and temperature distribution in high speed preloaded ball screws," Key Engineering Materials, **572**(1), pp. 363-366.

[25] Mao, X., Mao, K., Wang, F., Yan, B., Lei, S., 2018, "A convective heat trasfer coefficient algorithm for thermal analysis of machine tools considering a temperature change", International Journal of Advanced Manufacturing Technology, **99**(1), pp. 1877-1889.

[26] Siemens, Synchronous motors SINAMICS S110 / S120, 2018.

[27] O'Hara, P., Duarte, C. A., & Eason, T. (2011). "Transient analysis of sharp thermal gradients using coarse finite element meshes." Computer Methods in Applied Mechanics and Engineering, 200(5-8), pp. 812-829.

Figure Captions List

Fig. 1 Experimental procedure flow-chart

Fig. 2 Working center with three CNC stations: the rectangular shapes represent the critical zones where the measurements were made for the thermal passive (TP) model. (b) Single 3-axes CNC station in the testing room: the characteristic zones where the thermal measurements were made are highlighted for the thermal dynamic (TD) model.

Fig. 3 A quarter of the entire work center was split into two macro-zones

Fig. 4 The roller monoguides in a single 3-axis CNC module, highlighted in yellow

Fig. 5 Example of load distribution on a couple of roller monoguides (Fload is represented by red arrows, Fpr by blue arrows)

Fig. 6 The Ball-screws in a single 3-axis CNC module, highlighted in yellow

Fig. 7 Axis motor in a single 3-axis CNC module, highlighted in yellow

Fig. 8 Meshed quarter of the entire machining center. The highlighted sheet metal case was meshed by manual sizing method

Fig. 9 Global thermal trend of the critical areas (represented in Fig. 2) with environment temperature trend

Fig. 10 Experimental and simulated (before and after calibration) temperature values during a working day in distinct zone TP 2

Table Caption List

Table 1 Theoretical coefficients for laminar flow in the different zones used for the first simulation model and corrected coefficient obtained after the tuning process

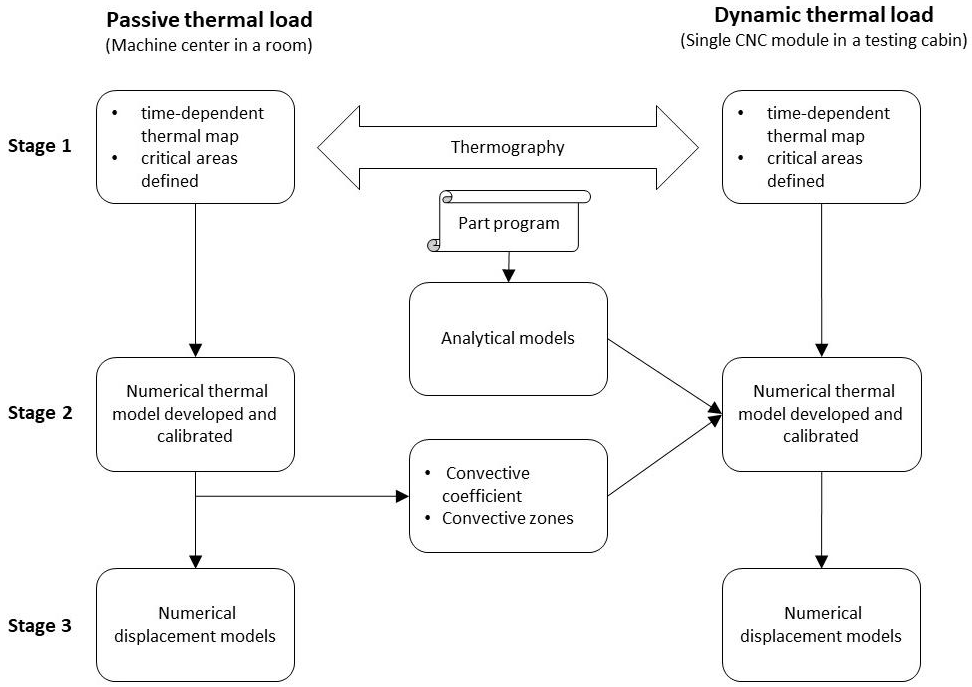

Fig. 1: Experimental procedure flow-chart.

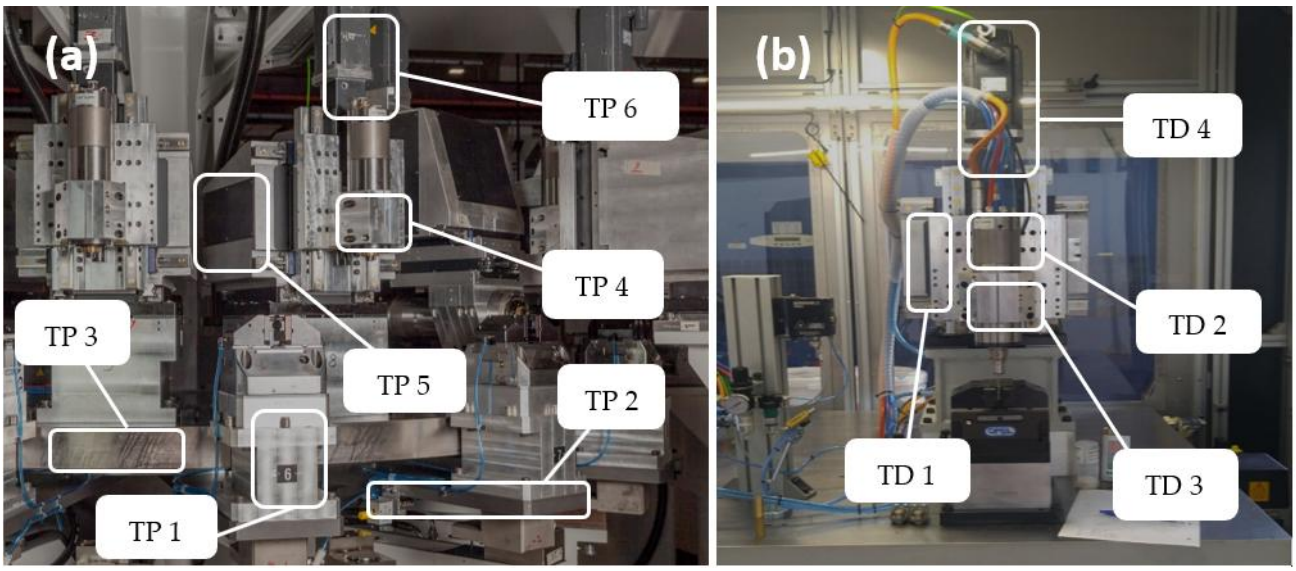

Fig. 2: (a) Working center with three CNC stations: the rectangular shapes represent the critical zones where the measurements were made for the thermal passive (TP) model. (b) Single 3-axes CNC station in the testing room: the characteristic zones where the thermal measurements were made are highlighted for the thermal dynamic (TD) model.

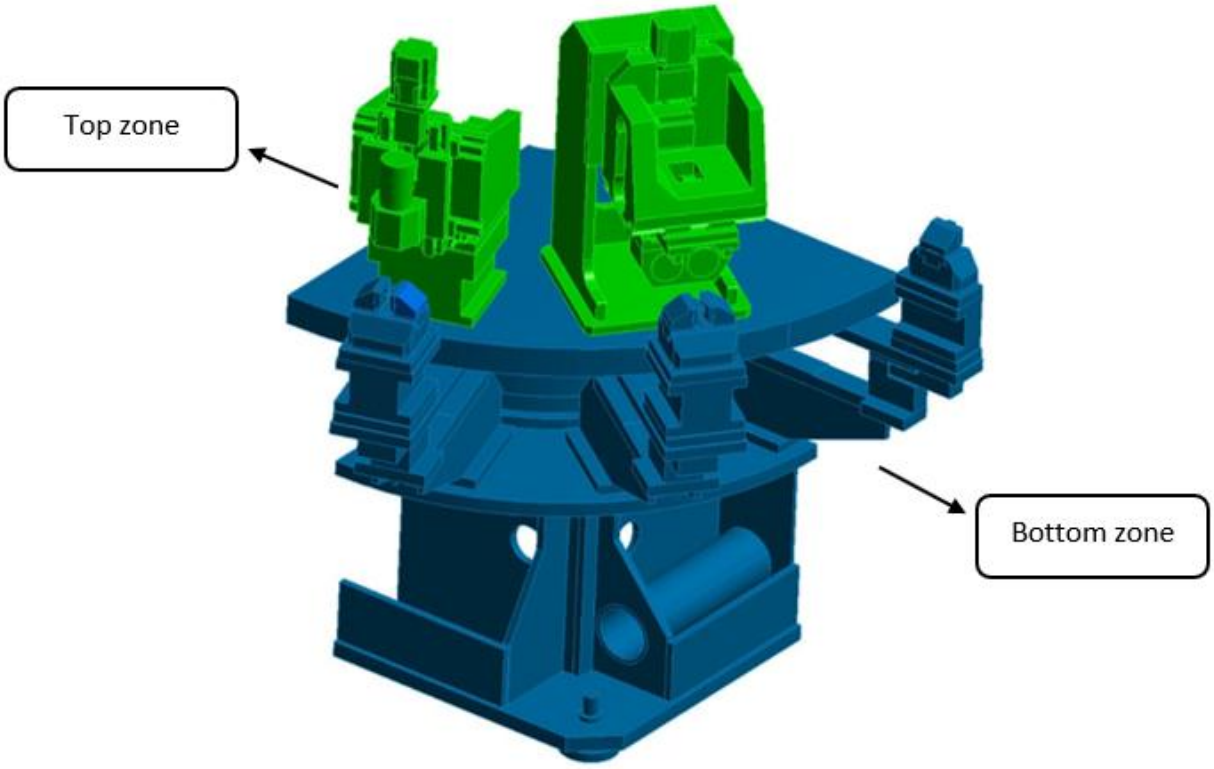

Fig. 3 – A quarter of the entire work center was split into two macro-zones.

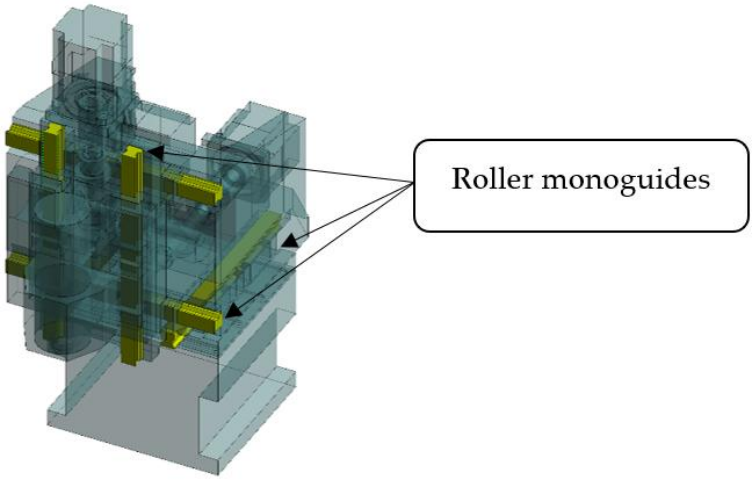

Fig. 4 – The roller monoguides in a single 3-axis CNC module, highlighted in yellow.

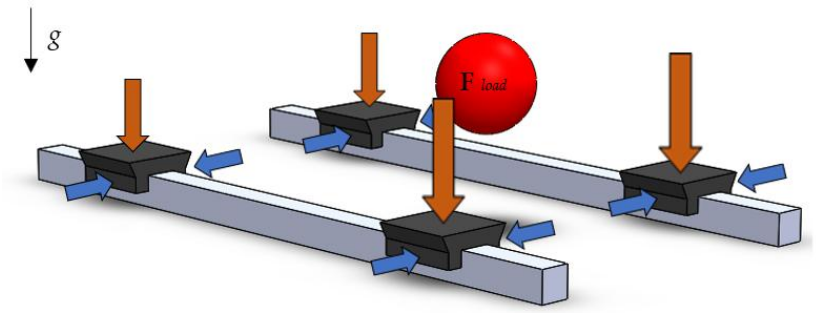

Fig. 5 - Example of load distribution on a couple of roller monoguides (Fload is represented by red arrows, Fpr by blue arrows).

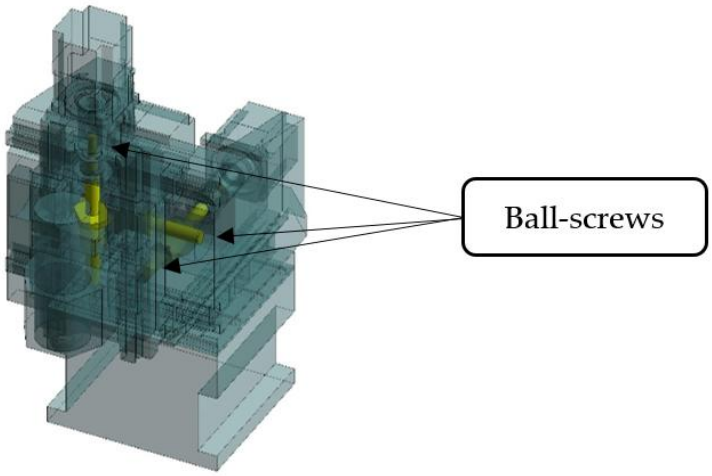

Fig. 6 - The Ball-screws in a single 3-axis CNC module, highlighted in yellow.

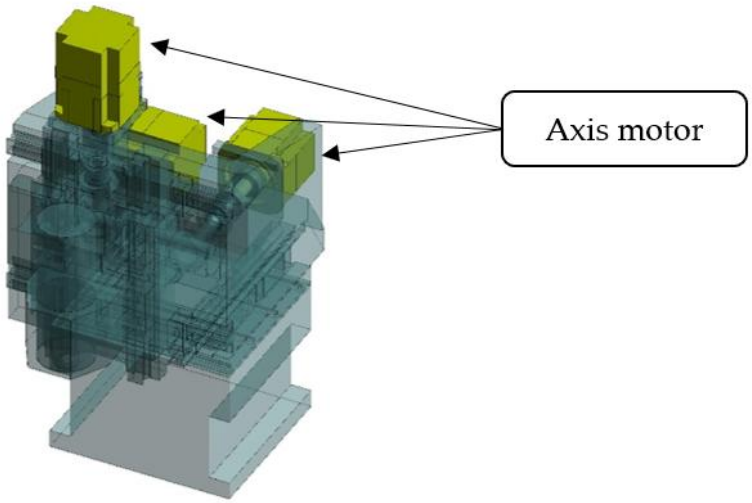

Fig. 7 - Axis motor in a single 3-axis CNC module, highlighted in yellow.

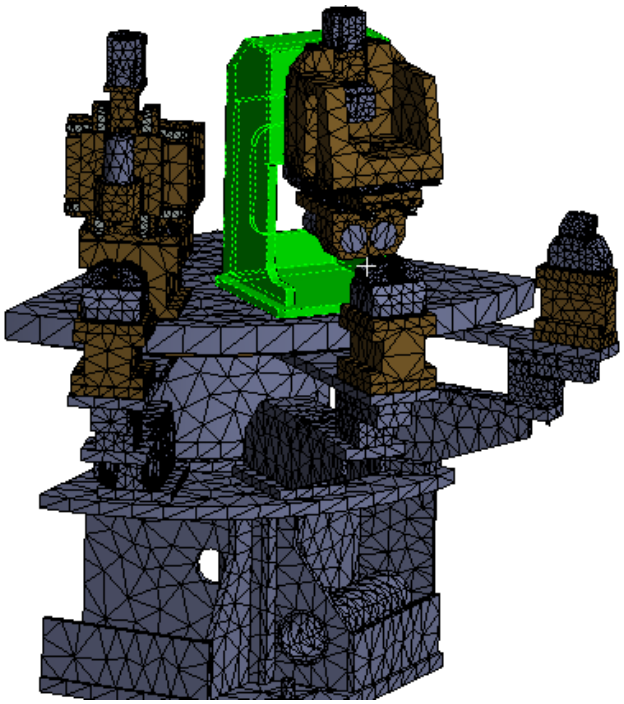

Fig. 8 – Meshed quarter of the entire machining center. The highlighted sheet metal case was meshed by manual sizing method.

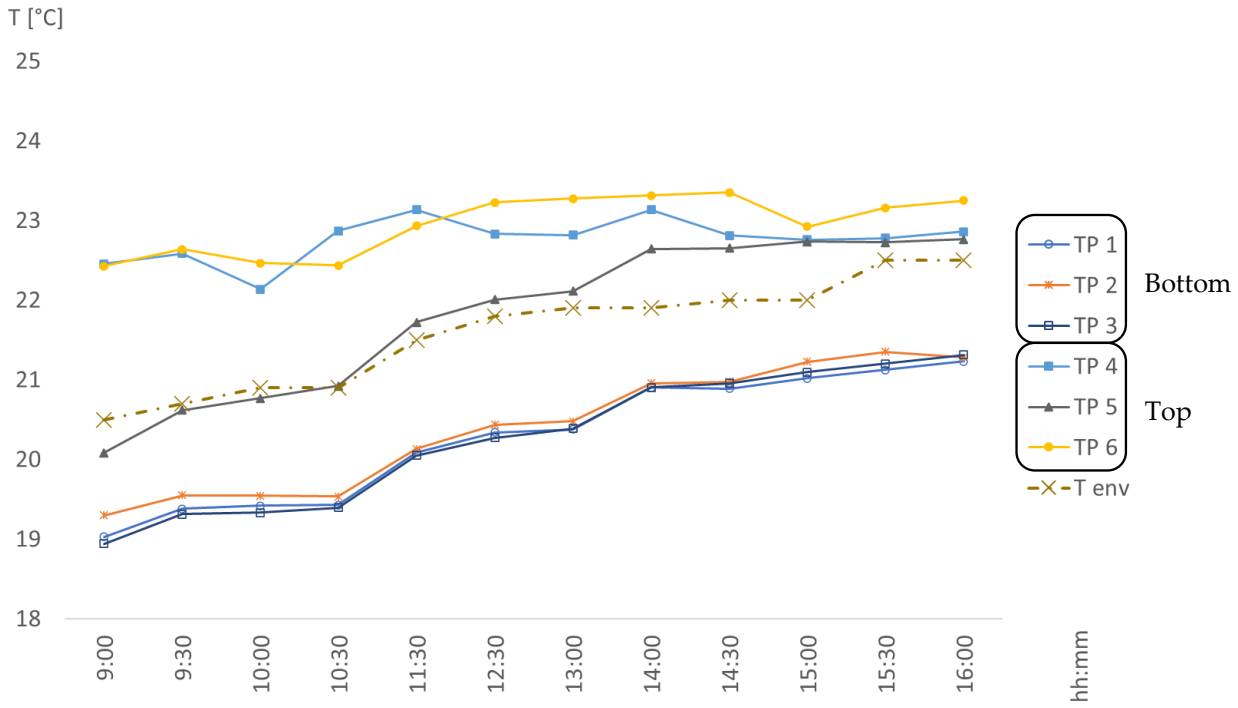

Fig. 9: Global thermal trend of the critical areas (represented in Fig. 2) with environment temperature trend.

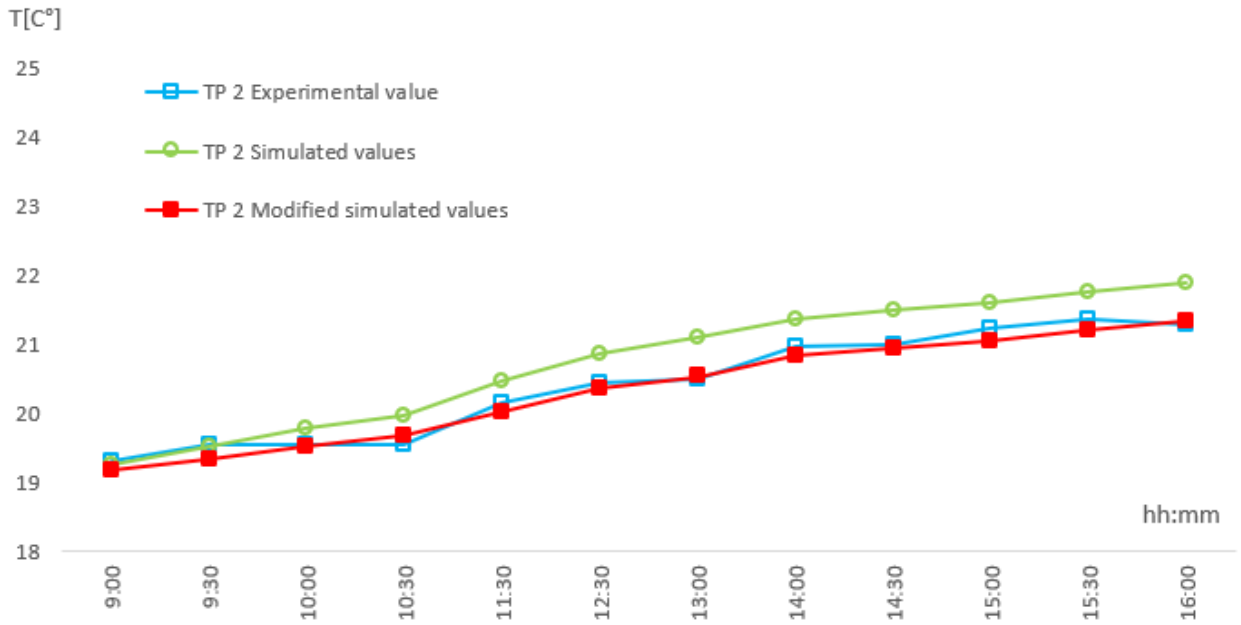

Fig. 10: Experimental and simulated (before and after calibration) temperature values during a working day in distinct zone TP 2.

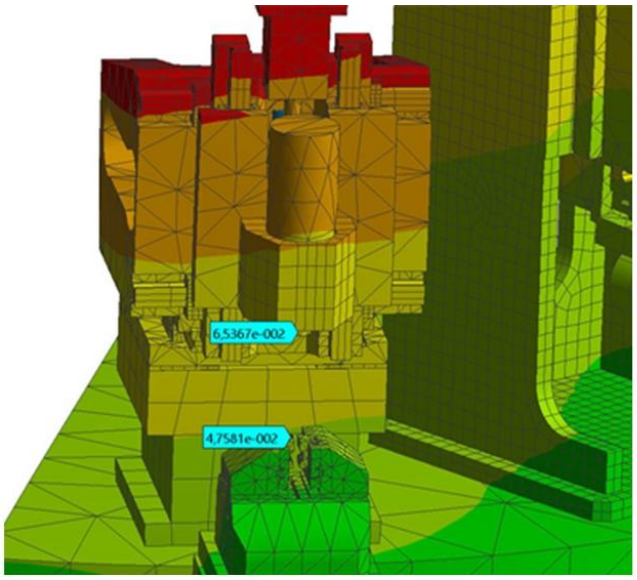

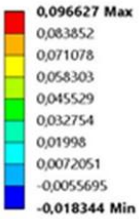

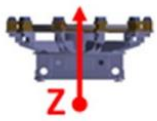

Axial deformation (ΔT_{env}~3 C° in 8h)		Relative displacement
Spindle nose	0,065 (mm)	0,017 (mm)
Clamp	0,048 (mm)	

Fig. 11: Vertical displacement (z axis) results.

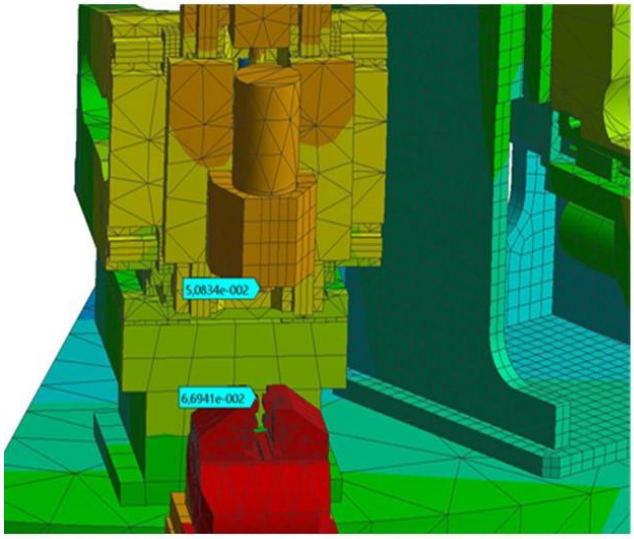

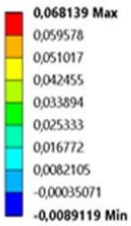

Radial deformation (ΔT_{amb}~3 C° in 8h)		Relative displacement
Spindle nose	0,051 (mm)	0,016 (mm)
Clamp	0,067 (mm)	

Fig. 12: Radial displacement (x axis) results.

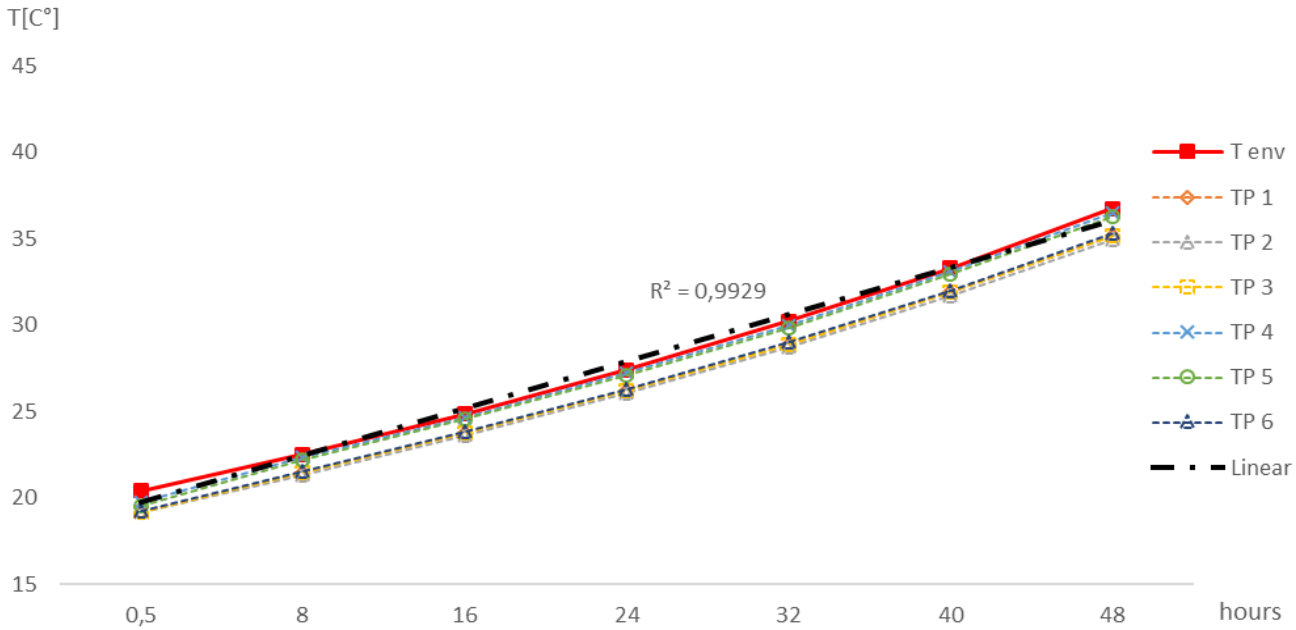

Fig. 13: Global trend of the thermal critical areas highlighted in Fig. 1.

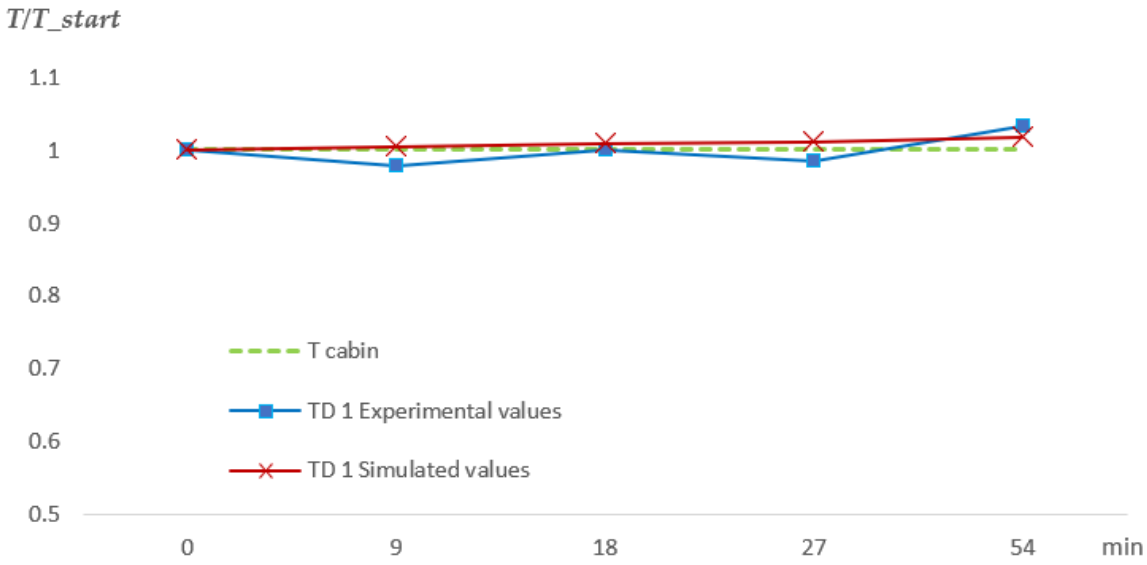

Fig. 14: Comparison between the experimental and numerical yields with regard to thermal dynamic zone 1 (TD 1).

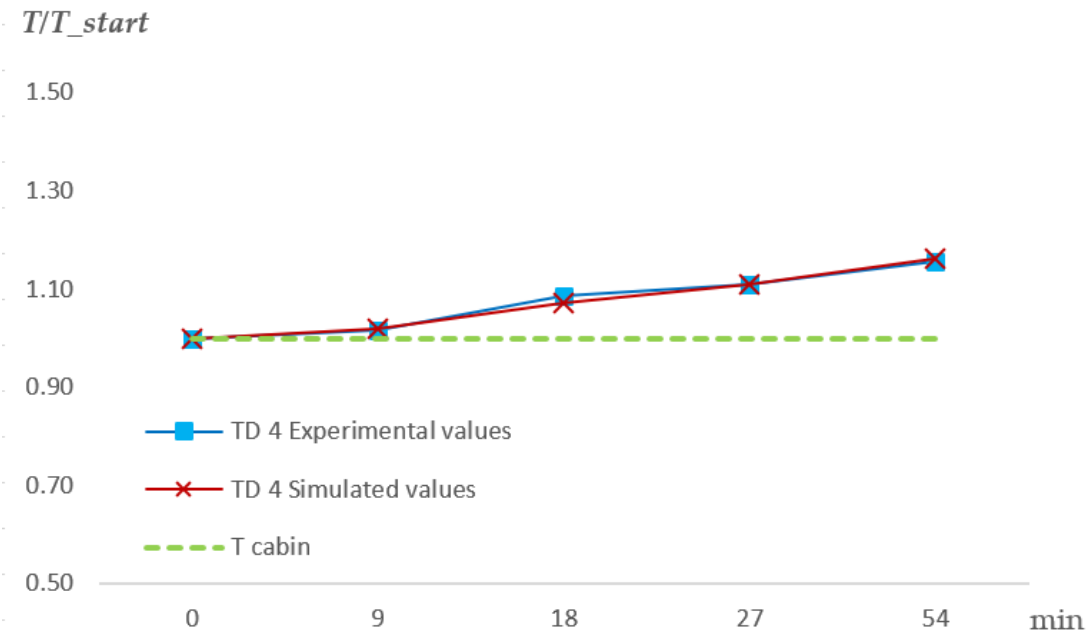

Fig. 15: Comparison between the outcomes of the experimental and numerical models of the thermal dynamic zone 4 (TD 4).

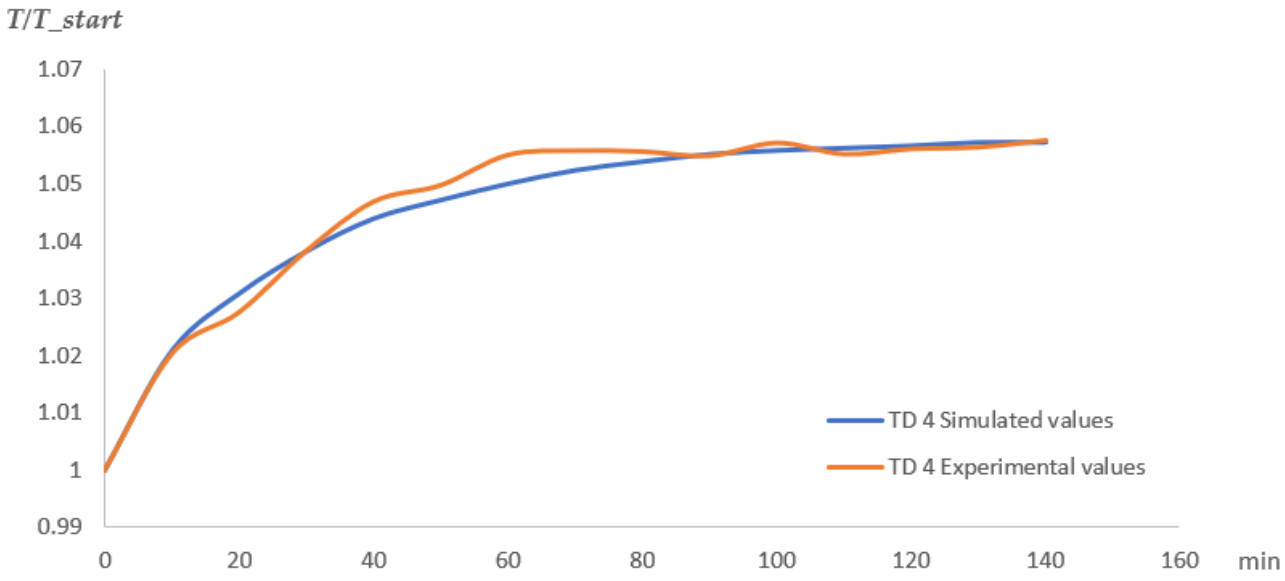

Fig. 16: Thermal dynamic zone TD 4 temperature: comparison between the experimental and the numerical results for the extended duration warmup test (140 minutes).

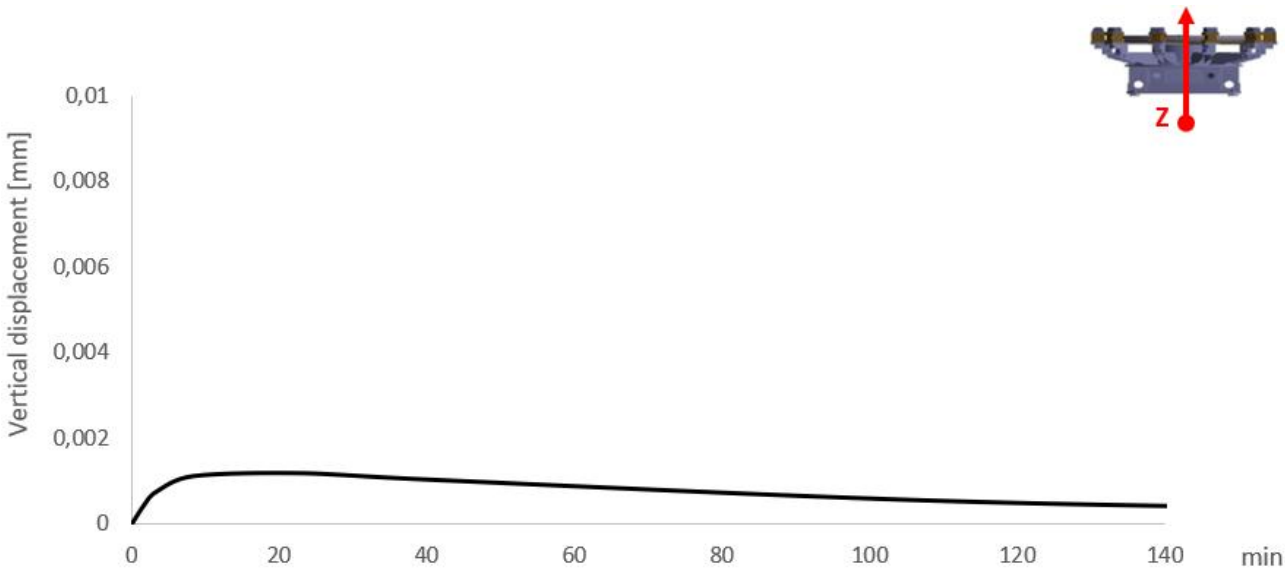

Fig. 17: Structural analysis results in terms of relative vertical displacement.

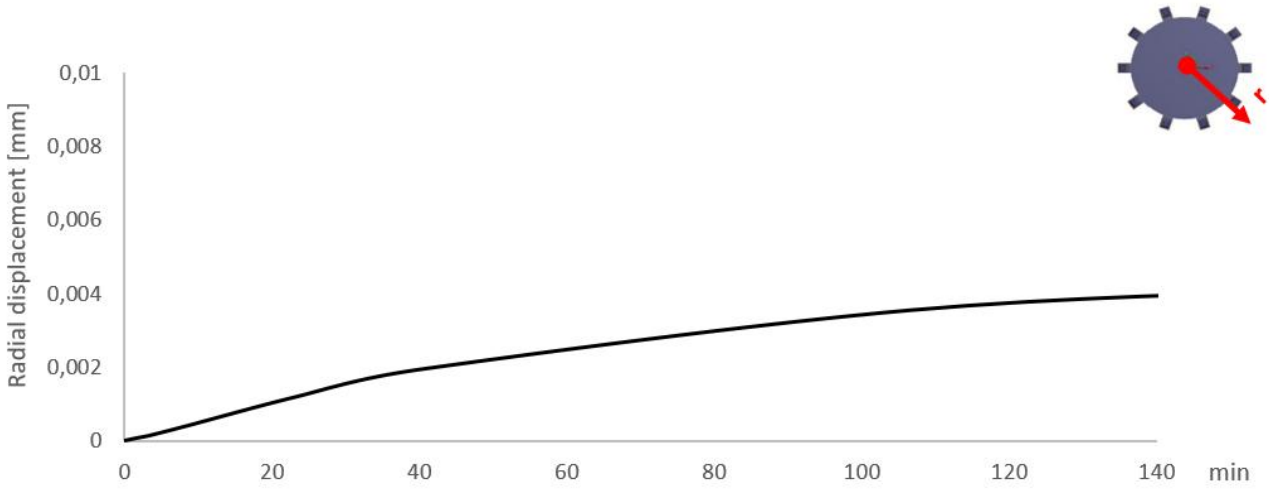

Fig. 18: Structural analysis results in terms of relative radial displacement.

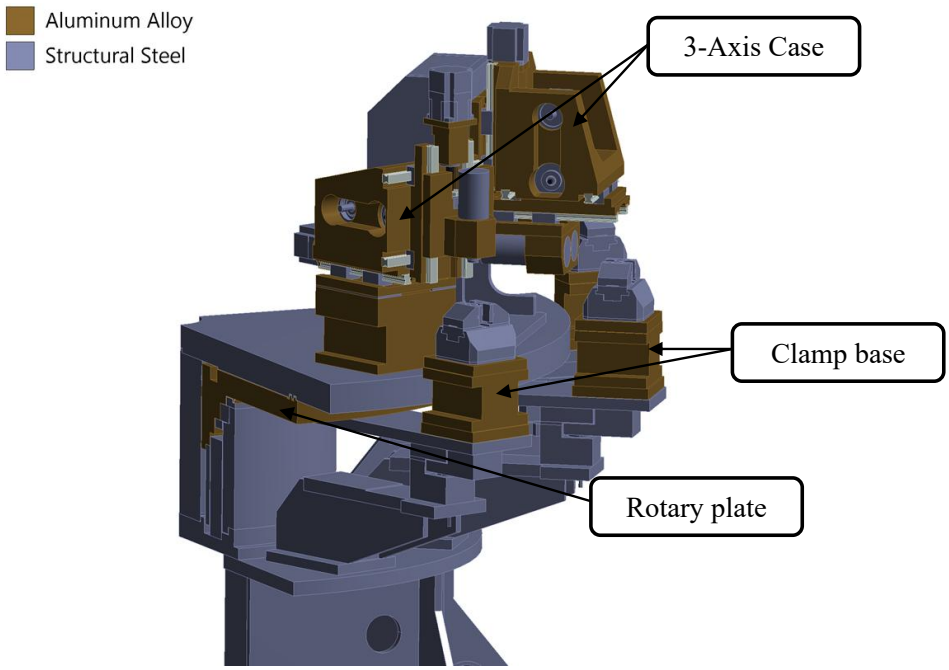

Figure 19 - A section view of the machining center, which highlights the materials used for the components.

Table 1 Theoretical coefficients for laminar flow in the different zones used for the first simulation model and corrected coefficient obtained after the tuning process

Zone	Initial air calm coefficient	Corrected air calm coefficient
Top zone	$5\ W/m^2K$	$25\ W/m^2K$
Bottom zone	$5\ W/m^2K$	$3\ W/m^2K$